Forging inner-disk Al-rich chondrules by interactions of CAI-like melt and ambient gas

Mingming Zhang[a*], Kohei Fukuda[a†], Michael J. Tappa[b], Guillaume Siron[c], William O. Nachlas[b], Makoto Kimura[d], Kouki Kitajima[a], Ann M. Bauer[b], Noriko T. Kita[a]

[a] *WiscSIMS, Department of Geoscience, University of Wisconsin–Madison, Madison, WI 53706, USA*

[b] *Department of Geoscience, University of Wisconsin–Madison, Madison, WI 53706, USA*

[c] *Laboratoire Chrono-Environnement, Université de Franche-Comté, UMR 6249, 25000 Besançon, France*

[d] *National Institute of Polar Research, Meteorite Research Center, Midoricho 10-3, Tachikawa, Tokyo 190-8518, Japan*

[*] *Corresponding address:* mzhang467@wisc.edu

[†] *Present address: Graduate School of Science, Osaka University, 1-1 Machikaneyama-cho, Toyonaka, Osaka 560-0043, Japan*

ABSTRACT

The mechanism of gas-melt interactions and the compositions of precursors are key to understanding the formation of chondrules. To shed light on the two enigmas, we studied the petrography, chemistry, and oxygen isotopes of six Al-rich chondrules (ARCs, five glassy and one plagioclase-bearing) in unequilibrated ordinary chondrites (OCs, petrologic subtype: 3.05). The plagioclase-bearing ARC was also investigated with Al-Mg chronology. Elemental zonation and inter-element correlations in glassy mesostasis of two ARCs indicate the condensation of gaseous Mg, SiO, Fe, and Na onto chondrule melt. The plagioclase-bearing ARC appears to display internal mass-independent oxygen isotope fractionation with $\delta^{18}O$ increasing following the order of mineral crystallization, suggesting partial oxygen isotope exchange with ambient gas during crystallization. Oxygen isotopes of the six ARCs are distributed along a mixing line of slope = 0.99 ± 0.05, which intersects with calcium-aluminum-rich inclusions (CAIs), consistent with a small portion of OC type IA chondrules, but deviates from other OC ferromagnesium chondrules (FMCs) towards higher $\delta^{17}O$, suggesting that OC ARCs and some IA chondrules were established by interactions between CAI-like melts and ^{16}O-poor ambient gas, rather than simply remelting solid mixtures of CAI and FMC materials.

All ARCs have unfractionated refractory lithophile element patterns with bulk concentrations ranging from ~7 × CI to ~15 × CI, indicating ~30-100 % of CAI-like materials in their precursors. Their bulk compositions are linearly evolved toward the Mg: SiO ~ 3:2 to 2:1 (in atomic) apex, consistent with adding gaseous Mg and SiO to the chondrule bulk via gas-melt interactions. The back-calculated compositions of the recycled CAI-like materials closely overlap with pyroxene-anorthite-rich CAIs, suggesting that extensive interactions between the melt of pyroxene-anorthite-rich CAI-like materials and ambient gas could make OC ARCs. The Al-Mg age of the plagioclase-bearing ARC is ~2.2 Ma after CAIs, similar to typical OC FMCs, suggesting that the refractory component arrived in the OC reservoirs at the end of the chondrule heating events.

Keywords: Al-rich chondrules; gas-melt interactions; Ca-Al-rich inclusions; ordinary chondrites.

1. Introduction

Chondrules are considered to form in dust-rich environments where interactions between chondrule melts and ambient gas are highly frequent (Cuzzi and Alexander, 2006; Alexander et al., 2008). The gas-melt interactions play a fundamental role in shaping the petrographic, chemical, and isotopic features of chondrules. Petrographically, interactions with gaseous Mg and SiO resulted in the formation of mineralogically-zoned chondrules (low-Ca pyroxene rim with an olivine-rich core; e.g., Tissandier et al., 2002; Friend et al., 2016; Barosch et al., 2019) and near-equilibrium epitaxial growth bands in magnesium-rich olivine (Libourel and Portail, 2018; Marrocchi et al., 2018, 2019; Piralla et al., 2021). Chemically, the condensation of gaseous Mg and SiO onto chondrule melt modified the bulk compositions of initial chondrule melts and contributed to the establishment of major element zonation in chondrule mesostasis (e.g., Libourel et al., 2006; Nagahara et al., 2008). Isotopically, the limited mass-dependent fractionation of isotopes of moderately volatile elements suggests chondrule melt evaporation was suppressed by high partial pressures of these elements in ambient gas and possibly buffered by recondensation processes (e.g., Galy et al., 2000; Tachibana and Huss, 2005; Alexander et al., 2008; Russell et al., 2018; Kadlag et al., 2019, 2021; Villeneuve et al., 2020; Martins et al., 2021). Meanwhile, the common oxygen isotope homogeneity (indicates homogeneous in both $\delta^{18,17}O$ and $\Delta^{17}O$; $\Delta^{17}O = \delta^{17}O - 0.52 \times \delta^{18}O$) among minerals and glass in chondrules indicates that oxygen isotope exchanges between chondrule melt and ambient gas was efficient (e.g., Kita et al., 2010; Ushikubo et al., 2012; Tenner et al., 2015; Zhang et al., 2022).

However, the mechanism of gas-melt interactions during chondrule formation remain poorly understood, partially due to the subsequent melt crystallization process and asteroidal thermal metasomatism that modified their element distributions and mineral chemistries. In contrast to typical ferromagnesium chondrules (FMCs), Al-rich chondrules (ARCs, bulk Al_2O_3 ≥ 10 wt%) in unequilibrated ordinary chondrites (OCs) typically contain abundant glassy mesostasis in addition to olivine, high-Ca pyroxene, and occasionally, spinel (e.g., Bischoff and Keil, 1984; Ebert and Bischoff, 2016). The glassy mesostasis in OC ARCs records primary information about the elemental exchange processes between chondrule melt and ambient gas. Direct evidence for the condensation

of gaseous Mg, SiO, and alkali elements is supported by concentric zonation of major elements across glassy mesostasis (Nagahara et al., 2008). Furthermore, the significant Al-rich nature of the chondrule melt recorded internal heterogeneity in the mass-independent fractionation of oxygen isotope indicative of partial exchange with ambient gas (Russell et al., 2000; Jiang et al., 2015; Ebert et al., 2022), different from typical OC FMCs that display oxygen isotope homogeneity (Kita et al., 2010; Piralla et al., 2021; Siron et al., 2021, 2022). Thus, a combined chemical and oxygen isotope study of ARCs in the least metamorphosed OCs would further elucidate the characteristics of gas-melt interactions.

After revealing the effect of gas-melt interactions on chondrule bulk compositions, the initial compositions of chondrule melts (precursor) could be interpreted. Major- and trace-element compositions of OC ARCs show enrichments in Al_2O_3 and other refractory lithophile elements (RLEs) that occasionally display group II/III rare earth element (REE) patterns (e.g., MacPherson and Huss, 2005; Ebert and Bischoff, 2016), suggesting the existence of refractory calcium-aluminum-rich inclusion (CAI)-like materials among their precursors. This argument is further supported by their oxygen isotope ratios ($\delta^{17,\,18}O$ down to ~ –15 ‰), which are relatively more ^{16}O-enriched than typical FMCs ($\delta^{17,\,18}O$ > 0 ‰) towards those of CAIs ($\delta^{17,\,18}O$ ~ –45 ‰) (Russell et al., 2000; Jiang et al., 2015; Ebert et al., 2022). However, the negative or near-zero $\varepsilon^{50}Ti$ in OC ARCs argues against this refractory component being a typical CAI ($\varepsilon^{50}Ti$: +2 to +12); instead, it is more likely derived from a ^{50}Ti excess-free CAI-like component that existed exclusively in the inner disk (Ebert et al., 2018).

Here we present petrography, mineral chemistry, bulk major- and trace-element compositions, and oxygen isotopes of six OC ARCs; of which, one was also investigated with Al-Mg chronology. This work differs from previous studies on ARCs which are mainly from metamorphosed type 3.1-4 OCs (Russell et al., 1996, 2000; MacPherson and Huss, 2005; Jiang et al., 2015; Ebert and Bischoff, 2016; Ebert et al., 2022). Instead, our study focuses on ARCs in pristine OCs with petrologic types of 3.05, where their mineral chemistries, elemental distributions, and oxygen and magnesium isotope systems remain largely undisturbed. The results provide critical information on

gas-melt interaction mechanism during the formation of OC ARCs and the nature of their refractory precursors.

2. Analytical methods

2.1 Sample descriptions and electron microprobe analyses

Eight polished sections of six OCs studied by Siron et al. (2021, 2022), i.e., NWA 7731 (L3.00), NWA 8276 (L3.00), NWA 8649 (LL3.05), QUE 97008 (L3.05), MET 00452 (L/LL 3.05), and MET 00526 (L/LL 3.05), were surveyed for ARCs. Based on the iron-rich olivine compositions (Cr_2O_3 contents; Grossman and Brearley, 2005) and the Fe-Ni metal texture and chemistry (Kimura et al., 2008), these OCs are interpreted to be pristine that experienced minimal asteroidal thermal metamorphism (Agee et al., 2013; Ruzicka et al., 2017; Siron et al., 2022). We note that NWA 7731 and NWA 8276 are likely 3.05-3.1 according to Fe-Ni metal texture and chemistry (Siron et al., 2022) rather than 3.00 (Agee et al., 2013; Ruzicka et al., 2017). Thus, we consider them to be similar to the 3.05 UOCs. Of the ~3000 chondrules present in these sections, only six were found to be Al-rich: NWA 7731_A1, NWA 8276_A1 & A2, NWA 8649_A1, and MET 00526_A1 & A2.

Petrography of the six ARCs was examined using a Hitachi S3400 variable-pressure scanning electron microscope (SEM) at the Geoscience Department, University of Wisconsin-Madison (UW-Madison). Energy dispersive spectroscopy (EDS) X-ray elemental mapping was performed for MET 00526_A2, NWA 8276_A2, and NWA 7731_A1. Major and minor element concentrations of constituent phases of ARCs (spinel, olivine, pyroxene, plagioclase, glass, and microcrystalline mesostasis) were determined using a Cameca SXFive field-emission electron probe microanalyzer (FE-EPMA) at UW-Madison. Analyses were conducted with an accelerating voltage of 15 kV, beam current of 10-20 nA, and beam diameter ranging from ~200 nm (focused, for individual phases) to 15 μm (defocused, for mesostasis). Background correction was conducted by linear interpolation between high and low background positions. Counting times were 20 or 10 s on peak and 10 or 5 s on each background position. A time-dependent intensity correction was applied for Na in glass. Interference corrections were applied for interference of V Kα by Ti Kβ and Cr Kα by V Kβ.

Each phase was analyzed with a specific set of elements that were calibrated using standards of high-purity natural or synthetic minerals, oxides, or glasses. The analytical details of beam conditions, detection limits, and calibration standards for each phase are in Table S1. Data acquisition and processing was performed using Probe for EPMA analytical software.

2.2 SIMS oxygen three-isotope analyses

The oxygen three-isotope ratios of constituent phases in ARCs were determined using the CAMECA IMS-1280 at the WiscSIMS lab of UW-Madison. The measurements were conducted in two sessions using multi-collection Faraday Cup (MCFC) and multi-collection FC and electron multiplier (FC-EM). The analytical condition of the MCFC session is similar to those described in Kita et al. (2010) and Zhang et al. (2022). A focused $^{133}Cs^+$ primary beam with a size of ~12 μm and beam intensity of ~2 nA was used. The typical count rate for $^{16}O^-$ was (2-3) × 10^9 cps (counts per second). Secondary ions $^{16}O^-$, $^{17}O^-$, and $^{18}O^-$ were detected simultaneously using three FCs with feedback resistors of 10^{10} ohm, 10^{12} ohm, and 10^{11} ohm, respectively. The utilization of a 10^{12} ohm resistor reduced thermal noise for FC and significantly improved analytical precision for $\delta^{17}O$ (Goodrich et al., 2019; Bouden et al., 2021; Zhang et al., 2022). The analytical condition of the FC-EM session is similar to those described in Ushikubo et al. (2012), during which additional analyses on MET 00526_A2 were made. A primary ion beam was focused to ~3 μm in size with an intensity of ~20 pA. The typical count rate for $^{16}O^-$ was (2-3) × 10^7 cps. Secondary ion $^{16}O^-$ was detected using an FC with a resistor of 10^{11} ohm, while $^{17}O^-$ and $^{18}O^-$ were detected using EMs. In both sessions, mass resolving power (MRP) was set to ~5000 for $^{17}O^-$, under which the peaks of $^{17}O^-$ and $^{16}OH^-$ were sufficiently resolved. The count rate of $^{16}OH^-$ was measured at the end of each measurement, and the contribution of its tailing on $^{17}O^-$ was corrected using the method described in Heck et al. (2010).

Each set of 15-20 measurement of unknown samples was bracketed by eight analyses (four before, four after) on San Carlos olivine (SC-Ol), giving spot-to-spot reproducibility (2SD, standard deviation) for $\delta^{18}O$, $\delta^{17}O$, and $\Delta^{17}O$ of ~0.25 ‰, ~0.3 ‰, ~0.3 ‰, respectively, in the MCFC session,

and of ~0.5 ‰, ~1.0 ‰, ~1.0 ‰, respectively, in the FC-EM session. The instrumental bias of spinel, olivine, pyroxene, plagioclase, and glass in these ARCs was corrected using reference materials (RM) that generally cover their compositional ranges (listed in Table S4). For glass and high-Ca pyroxene in glassy ARCs, which are significantly richer in Al_2O_3 than the glass and diopside compositions of the RMs used, an additional 0.5 ‰ and 0.25 ‰ uncertainties of instrumental bias corrections were applied empirically to their $\delta^{18}O$ and $\delta^{17}O$, respectively. Following analysis, the SIMS pits were carefully examined with BSE imaging and EDS measurements using the Hitachi S3400 SEM (supplementary material 1). Data obtained from pits overlapping nearby or subsurface phases and cracks were rejected. If multiple analyses on a chondrule show indistinguishable oxygen isotope ratios, the mean values ("host chondrule") were calculated (Table S5-6). The uncertainty of mean values was calculated following the reduction scheme described in Hertwig et al. (2018).

2.3 SIMS Al-Mg isotope analyses

The Al-Mg isotope analyses of major minerals in MET 00526_A2 were performed using the CAMECA IMS-1280 SIMS equipped with a radio-frequency (RF) plasma ion source in two sessions: MCFC for spinel and olivine and FC-EM for plagioclase. The power of the RF source was set to 700 W. The analytical conditions for both sessions are similar to those described in Fukuda et al. (2020) and Siron et al. (2021). For both sessions, a $^{16}O^-$ primary ion beam with an intensity of ~0.5 nA and a size of 6 μm was used.

In the MCFC session for spinel and olivine, secondary ions $^{24}Mg^+$, $^{25}Mg^+$, and $^{26}Mg^+$ were counted using FCs with a resistor of 10^{12} ohm, and $^{27}Al^+$ was counted simultaneously using an FC with a resistor of 10^{11} ohm. The typical count rate for $^{24}Mg^+$ was (2-4) × 10^7 cps. Each analysis took ~10 min, including 100 s of presputtering, ~80 s for secondary ions centering, and 500 s for ion signal integration (10 s × 50 cycles). The instrumental biases of spinel and olivine were corrected with a natural Mg-Al-spinel RM (Mg isotopes unknown, $\delta^{26}Mg$ and $\delta^{25}Mg$ assumed to be 0 ‰; Kita et al., 2012) and a synthetic forsterite RM (HN-Ol) with known Mg isotope ratios (Fukuda et al., 2020), respectively. The relative sensitivity factor (RSF), the SIMS-measured $^{27}Al/^{24}Mg$ ratio relative to that

176 measured with EPMA, of spinel was also corrected (Kita et al., 2012). Since Al_2O_3 in olivine standard
177 is too low to be accurately determined by EPMA under these conditions, RSF of orthopyroxene
178 standard was determined in the same session and applied to olivine (Ushikubo et al., 2013).
179 In the FC-EM session for plagioclase (0.8-1.0 wt% MgO, as determined by EPMA),
180 secondary ions $^{24}Mg^+$ (5-8 × 10^5 cps) and $^{27}Al^+$ (5-8 × 10^7 cps) were counted using two FCs with
181 resistors of 10^{12} ohm and 10^{11} ohm, respectively, while $^{25}Mg^+$ and $^{26}Mg^+$ (~1 × 10^5) were detected
182 using two EMs. The analysis time was ~32 min, including 120 s of presputtering and FC baseline
183 measurement (for $^{24}Mg^+$), ~80 s for secondary ions centering, and 1600 s for ion signal integration (4
184 s × 400 cycles). To maintain constant EM gains relative to the FC detectors during this long data
185 acquisition period, the high voltage of each EM was adjusted at the 20th and 220th cycles using a
186 Cameca software routine. The gain drift for each EM was monitored and corrected using a second
187 discriminator connected parallel to the first one, as described in supplementary material 2 of Siron et
188 al. (2021). The instrumental biases and RSF of plagioclase was corrected using two anorthitic glass
189 standards with MgO contents of 0.5 wt% and 1.0 wt%, respectively (Kita et al., 2012).
190 The measured $^{25}Mg/^{24}Mg$ and $^{26}Mg/^{24}Mg$ ratios were normalized by the absolute Mg isotope
191 ratios (0.12663 and 0.13932, Catanzaro et al. (1966)) and expressed as delta notations $\delta^{25}Mg$ and
192 $\delta^{26}Mg$, respectively. The excess $\delta^{26}Mg^*$, corresponding to the fraction of ^{26}Mg due to the decay of
193 ^{26}Al, was calculated as a function of the instrumental bias-corrected $\delta^{25}Mg$ and $\delta^{26}Mg$ values:

194 $$\delta^{26}Mg^* = [(1+\frac{\delta^{26}Mg}{1000}) - (1+\frac{\delta^{25}Mg}{1000})^{\frac{1}{\beta}}] \times 1000 = \Delta^{26}Mg \times (1+\frac{\delta^{25}Mg}{1000})^{\frac{1}{\beta}}$$

195 where the $\Delta^{26}Mg$ is the mass-independent fractionation term and the β is the power of the mass
196 fractionation law that is assumed to be 0.5128 (Davis et al., 2015) for plagioclase, spinel, and olivine.
197 The term $\Delta^{26}Mg$ is nearly equal to $\delta^{26}Mg^*$ when the natural mass-dependent fractionation measured
198 as $\delta^{25}Mg$ in chondrules is small (≤1‰; Ushikubo et al., 2017; Tenner et al., 2019). Typical external
199 reproducibility (2SD) of the raw measured $\delta^{25}Mg$, $\delta^{26}Mg$, and $\Delta^{26}Mg$ for spinel RM were 0.12 ‰,
200 0.20 ‰, 0.09 ‰, for HN-Ol were 0.07 ‰, 0.06 ‰, 0.15 ‰, and for anorthitic glass (1 wt% MgO) were
201 0.36 ‰, 0.30 ‰, 0.79 ‰, respectively.

The initial $^{26}Al/^{27}Al$ ratios ($(^{26}Al/^{27}Al)_0$) of MET 00526_A2 were obtained from an isochron regression using Isoplot 4.15 (Model 1; Ludwig, 2012). Uncertainties for the reported $(^{26}Al/^{27}Al)_0$ values and relative ages are 95 % confidence intervals. The relative age was calculated as:

$$\Delta t\ (Ma) = \ln\left[\frac{(\frac{^{26}Al}{^{27}Al})_{0,CAI}}{(\frac{^{26}Al}{^{27}Al})_{0,Chondrule}}\right] \times \frac{0.705}{\ln(2)}$$

using the canonical CV CAI $(^{26}Al/^{27}Al)_0$ of 5.25×10^{-5} (Jacobsen et al., 2008; Larsen et al., 2011) and the half-life of ^{26}Al (0.705 Ma, Nishiizumi, 2004).

2.4 LA-ICP-MS trace element analysis

After SIMS oxygen and Al-Mg isotope analyses, trace element concentrations of the six ARCs (mainly glassy/microcrystalline mesostasis or a mixture of mesostasis and high-Ca pyroxene) were determined by LA-ICP-MS in the ICP-TIMS lab at UW-Madison. A Teledyne-Photon Machines Analyte femtosecond laser equipped with a HelEx LA cell was operated at a wavelength of 266 nm and a pulse-width of ~150 fs. The laser spot size was controlled by an adjustable iris and produced ~20 μm diameter craters. During the trace-element analysis, the laser conditions used a pulse energy of ~10 mJ on the sample surface, 150 laser shots, and a 5 Hz repetition rate for a total ablation time of 30 s per analysis (pit depth ~7-8 μm on NIST 610). Helium (total flow rate ~ 0.35 L/min) was used as the carrier gas to transport ablated particles out of the ablation cell. A mixing cell was used upstream of the plasma to smooth the ablation signal, where additional Ar (1 L/min) and N_2 (5 mL/min) gases were introduced. Laser parameters and flow rates were tuned prior to use by ablating NIST 610. The ablated particles were analyzed on Agilent 8900 QQQ ICP-MS. The ICP-MS was tuned using Agilent Tuning Solution sourced through an Aridus II desolvating nebulizer, and a pulse-to-analog calibration was made using in-house trace element solutions. The oxide production rate, monitored by CeO/Ce during tuning, was <0.02 ‰; therefore, no correction was applied. The instrument was operated in single quad mode and data was collected as a time-resolved analysis (TRA) with a total of 29 masses (^{28}Si, ^{29}Si, ^{45}Sc, ^{47}Ti, ^{51}V, ^{52}Cr, ^{55}Mn, ^{63}Cu, ^{66}Zn, ^{85}Rb, ^{88}Sr, ^{89}Y, ^{90}Zr,

^{137}Ba, ^{139}La, ^{140}Ce, ^{141}Pr, ^{146}Nd, ^{147}Sm, ^{153}Eu, ^{157}Gd, ^{159}Tb, ^{163}Dy, ^{165}Ho, ^{166}Er, ^{169}Tm, ^{172}Yb, ^{175}Lu, and ^{178}Hf) measured each at an integration time of 0.025 s for a total sampling period of 0.7574 s.

TRA data were processed using the "Iolite V4" software (Paton et al., 2011). ^{29}Si was used as an internal standard. The NIST SRM 612 (Pearce et al., 1997), USGS reference glass BIR-1G (REE ~ 5-10 × CI; Jochum et al., 2005) and MPI-DING reference glass GOR 128-G (REE ~ 0.5-9 × CI; Jochum et al., 2006) were used as running standards to bracket unknown sample analyses. Furthermore, the NIST SRM 610 and USGS reference glasses BCR-2G and BHVO-2G were also analyzed at the beginning of the session. Analytical uncertainties, evaluated by the RSDs (relative standard deviation between measured values and reference values) of the BIR-1G and GOR 128-G (Jochum et al., 2005, 2006), are typically <10 %. Following analysis, the laser pits were inspected by an optical microscope (supplementary material 1).

3. Results

3.1 Petrography

Plagioclase-bearing ARC; MET 00526_A2 (ellipsoidal-shaped, 430 × 250 μm) is the only ARC that contains abundant subhedral-euhedral plagioclase crystals (maximum dimension: ~45 μm) in this study. Other phases are spinel, olivine, high-Ca pyroxene, and mesostasis of microcrystalline plagioclase and high-Ca pyroxene (Fig. 1a). Spinel is a subhedral heart-shaped crystal (75 × 50 μm) located at the upper center of this chondrule. Olivine appears either as tablet crystals (up to 45 μm in length) scattered in the chondrule's interior or as anhedral crystals decorating its lower right surface (Fig. 1b). High-Ca pyroxene occurs as anhedral crystals between plagioclase laths. Scapolite (6-8 wt% Na_2O, 2-6 wt% Cl, ~0.7 wt% K_2O, 1-4 wt% FeO, 2-4 wt% CaO, 21-31 wt% Al_2O_3, 54-60 wt% SiO_2, determined by EDS) was identified along the grain boundaries, within the mesostasis, and pooled at the lower center of this chondrule (Fig. 1c). The crystallization sequence of minerals inferred from texture is spinel and olivine followed by plagioclase and high-Ca pyroxene, and then microcrystalline mesostasis.

Glassy ARCs; The remaining five ARCs of this study are round/ovoid-shaped with a size ranging from ~200 × 200 μm to ~1100 × 700 μm. They are dominated by Ca-Al-rich glass (NWA 8649_A1, NWA 7731_A1, and NWA 8276_A2, Figs. 1d, 2, 3) or slightly devitrified glass of microcrystalline high-Ca pyroxene and plagioclase (MET 00526_A1 and NWA 8276_A1, Fig. 1e-h). Glassy mesostasis is mostly isotropic, apart from that in NWA 8276_A2 (Fig. 2). The right portion of NWA 8276_A2 was replaced by an Mg-Al-Si-Ti-Fe-Ni-bearing hydrated phase (analysis total ~70 wt%), and its interior has mottled regions with micro-sized pores. Minerals embedded in glassy mesostasis are olivine, high-Ca pyroxene, and, occasionally, spinel. Olivine occurs typically as tablet or skeletal crystals scattered in chondrules' interior or located at chondrule peripheral with long axes parallel or perpendicular to their surfaces. In rare cases, olivine crystals align as parallel bars (NWA 8276_A1, Fig. 1g) or anhedral crystals decorating chondrule's surfaces (MET 00526_A1, Fig. 1e). High-Ca pyroxene commonly appears as dendritic crystals, especially in NWA 7731_A1 (~37.5 vol%). Meanwhile, it also occurs as diamond-shaped crystals with TiO_2 zonation (rim is enriched in TiO_2, Fig. 1f) and blocky crystals in MET 00526_A1. Spinel was found as a tiny (<10 μm) crystal at the center of NWA 7731_A1 (Fig. 3c) and coarse-grained (up to 70 × 35 μm) round crystals occasionally containing melt inclusions in NWA 8276_A1 (Fig. 1h).

3.2 Mineral & bulk major element abundances

Average major element compositions and modal abundances of constituent phases in the six ARCs and their bulk compositions are listed in Table 1. Individual major element analysis results are in Table S2. Mesostasis are Ca-Al-rich (13-19 wt% CaO, 19-26 wt% Al_2O_3) and MgO-poor (4-11 wt%), with minor amounts of Na_2O (typically <2.0 wt%, up to 3.3 wt%), TiO_2 (typically 0.8-1.2 wt%), Cr_2O_3 (<0.4 wt%), and FeO (typically <0.6 wt%, up to 3.6 wt%) and trace (<0.2 wt%) amounts of V_2O_3, MnO, and K_2O. The mesostasis of NWA 7731_A1 (high-Ca pyroxene-rich) is richer in SiO_2 (50-54 wt% vs. 46-52 wt%) than the others. Furthermore, the hydrated region (Fig. 2a) of NWA 8276_A2 is depleted in Na_2O (<0.1 wt% vs. <2.8 wt%), CaO (<1 wt% vs. 16-18 wt%), and Al_2O_3

(~10 wt% vs. 20-24 wt%) and enriched in FeO (~4 wt% vs. <0.6 wt%), NiO (~4 wt% vs. <0.1 wt%), and K_2O (~0.2 wt% vs. <0.03 wt%) compared to the interior pristine mesostasis.

Olivines grains are mostly forsteritic with Fo >99 and, in rare cases, contain > 1 wt% FeO (Fo_{97-99} in MET 00526_A1 and NWA 8276_A2). No chemical zonation of FeO was detected. Concentrations of CaO (0.3-0.7 wt%), Al_2O_3 (0.1-0.7 wt%), Cr_2O_3 (<0.3 wt%), TiO_2 (<0.2 wt%), NiO (<0.5 wt%), and MnO (<0.2 wt%) are minor. CaO in olivines of NWA 8276_A1 is systematically higher than in others (0.5-0.7 wt% vs. 0.3-0.5 wt%). Spinel grains are nearly pure Mg-Al-spinel. Compared to spinels in the glassy ARC NWA 8276_A1, the spinel crystal of plagioclase-bearing ARC MET 00526_A2 is richer in TiO_2 (~0.5 wt% vs. ~0.3 wt%) but poorer in FeO (~0.2 wt% vs. ~0.5 wt%), Cr_2O_3 (~0.2 wt% vs. ~0.3 wt%), and V_2O_3 (~0.2 wt% vs. ~0.4 wt%). In addition, plagioclase grains in MET 00526_A2 are anorthitic (An_{88-98}) with 0.8-1.0 wt% MgO and <1 wt% FeO. They have ≤0.7 mol% (mean value: 0.2) excess structural silica ($[]Si_4O_8$) component, as calculated using the algorithm described in Siron et al. (2021).

High-Ca pyroxenes in the glassy ARCs contain abundant Al_2O_3 (up to 17 wt%) that does not correlate with their TiO_2 contents; in contrast, in the plagioclase-bearing ARC MET 00526_A2, they have lower Al_2O_3 (3.8-7.0 wt%) that display a good correlation with TiO_2 (Fig. 4), similar to those in ARCs from CV chondrites (Zhang et al., 2020b). Cr_2O_3 (<0.6 wt%), FeO (typically <1.0 wt%), and V_2O_3 (<0.2 wt%) are minor, and Na_2O and MnO are almost absent (<0.1 wt%). The diamond-shaped high-Ca pyroxenes in MET 00526_A1 show normal TiO_2 zonation that increases outward from ~1.4 wt% to ~3.0 wt%.

Bulk major element compositions of the six ARCs were calculated by combining modal mineral abundances for individual chondrules with the average compositions of their constituent minerals (MacPherson and Huss, 2005). The modal mineral abundances are in mass fraction (wt%), which were converted from area fraction (assumed to be equivalent to the volume fraction) by multiplying the density of individual phases (Zhang et al., 2020b). The six ARCs contain 10-18 wt% CaO, 11-22 wt% Al_2O_3, 11-33 wt% MgO, 44-50 wt% SiO_2, 0.6-1.2 wt% TiO_2, <0.24 wt% Cr_2O_3, <0.07 wt% V_2O_3, <0.06 wt% MnO, and no K_2O. The $CaO+Al_2O_3+TiO_2$ abundance is lowest in the

olivine-rich ARC NWA 8276_A1 (~22 wt%) and goes up to ~32-38 wt% in other ARCs. Bulk Na_2O and FeO contents are typically <1 wt%, except for MET 00526_A2 (~1.5 wt%) which contains abundant scapolite in its microcrystalline mesostasis (analyzed with a defocused electron beam).

3.3 Mesostasis & bulk trace element abundances

Individual LA-ICP-MS analyses on mesostasis of three glassy ARCs (NWA 8276_A1, NWA 7731_A1, and NWA 8649_A1) show nearly uniform and unfractionated RLE (including REEs, Zr, Hf, Sc, Y, Ti, Sr, and Ba) abundances of 10-19 × CI, except for V that exhibits varying degrees of depletions (~0.4-3 × CI). Concentrations of moderately volatile elements (MVEs) Cr (~0.2-0.8 × CI), Mn (~0.1-0.4 × CI), and Rb (typically <0.5 × CI) decrease as their volatility increases (Fig. 5a, Table S3). The trace element patterns of mesostasis in NWA 8276_A2 are very similar to the above three ARCs (Fig. 5b), while concentrations of Rb are highly variable (<0.1-4 × CI). No correlation between trace element abundances and petrographic features, i.e., mottled mesostasis and clean glass, was identified. Blocky high-Ca pyroxene in MET 00526_A1 displays LREE-depletion with negative Eu anomaly and enrichments of Sc, Ti, and V (compatible elements), which are complementary to those in the microcrystalline mesostasis. Similarly, a scapolite-rich region of MET 00526_A2 (plagioclase-bearing) shows significantly depleted (~0.3-3 × CI, except Sr, Ba, and Eu) RLE abundances that are complementary to its microcrystalline mesostasis. But another scapolite-rich region shows indistinguishable trace element abundances from the mesostasis; both display a similar pattern to other glassy ARCs except for the depletion of Sr, Ba, and Eu due to the crystallization of plagioclase.

Bulk trace element compositions of the six ARCs were determined by multiplying the modal abundances of mesostasis and/or high-Ca pyroxene with their trace element concentrations determined by LA-ICP-MS (Table 2, Table S3). Additional corrections on bulk V, Cr, Ti, and Mn abundances were made by adding their concentrations in olivine and spinel determined by EPMA, which subtly affects the final totals. As a result, the six ARCs show unfractionated bulk RLEs abundances and volatility-dependent depletions of MVEs (V, Cr, Mn, and Rb). Due to the high

abundance of olivine, NWA 8276_A1 (MgO + SiO_2 = 77 wt%, ~7 × CI) has the lowest bulk concentrations of RLEs compared to the others (MgO + SiO_2 = 60-67 wt%, 10-15 × CI).

3.4 Major & trace element distributions in glassy mesostasis

Transverse EPMA major element and LA-ICP-MS trace element analyses were conducted across the glassy mesostasis of NWA 8276_A2 (Fig. 2c-d, supplementary material 1). MgO, TiO_2, and SiO_2 display chondrule-scale concentric zonation, in which MgO and TiO_2 monotonically decrease and SiO_2 increases from the center to the surface (Fig. 2e). Al_2O_3 content remains almost constant at the upper half of this chondrule (surface "A" to center in Fig. 2c) and shows symmetric zonation (23 wt% → 21 wt% → 24 wt%) at its lower half (center to surface "B" in Fig. 2c). A slight increase of Al_2O_3 and TiO_2 and a decrease of MgO and SiO_2 were observed near the central olivine (mostly plucked during sample preparation). While exhibiting minor irregularity, the FeO content shows an overall concentric zonation that increases outward from the center to the surface like SiO_2 (Fig. 2f). In contrast, CaO and Na_2O contents are complementary to each other without displaying chondrule-scale zonation. Na-rich zones generally bracket Na-poor zones, and a significant amount of Na is concentrated at the interface between the hydrated phase and interior glass (interpreted to be an alteration front) (Figs. 2d, f). On the other hand, transverse LA-ICP-MS analyses found weak symmetric zonation of V, Cr, and Mn in its upper mesostasis (surface A to center), while their profiles become irregular towards the lower surface B (Fig. S1). The Ti zonation profile determined by LA-ICP-MS is broadly similar to that determined by EPMA (Figs. 2e, S1). No chemical zonation of other RLEs (including REEs) were detected.

Transverse EPMA major element analyses were also performed for the mesostasis of NWA 7731_A1. Unlike NWA 8276_A2, its mesostasis displays localized symmetric zonation of MgO, SiO_2, Al_2O_3, and, to a weaker extent, TiO_2 (divided as segments I, II, III, and IV in Fig. 3e). The zonation patterns of segments I, II, and IV that are between high-Ca pyroxene branches are similar to the chondrule-scale zonation patterns observed in NWA 8276_A2, while segment III that crosses a coarse high-Ca pyroxene branch is opposite. In contrast, the FeO and Na_2O contents exhibit

concentric zonation across the entire chondrule (Fig. 3f). The peripheral ~100 μm region and several interior patches of this chondrule are richer in Na_2O, as illuminated by its X-ray elemental map of Na (Fig. 3d). The Na_2O and CaO abundances are in general complementary, with the latter showing larger variability due to high-Ca pyroxene crystallization.

3.4 Oxygen isotopes

A total of 43 analyses were performed on the six ARCs using a 12 μm primary beam (MCFC mode), and additional eight analyses were conducted on MET 00526_A2 using a 3 μm primary beam (FC-EM mode). Data from two analyses were rejected due to mixing with the adjacent chondrite matrix or another phase beneath (supplementary material 1). The results of oxygen isotope analyses on two ARCs (MET 00526_A2 and NWA 8649_A1) are variable, while others are homogeneous (Fig. 6, Table 3, S5-S6). The plagioclase-bearing ARC MET 00526_A2 displays the largest oxygen isotope variability, with $\delta^{18}O$ increasing in the order of spinel (~–10 ‰), olivine (~–9 ‰), high-Ca pyroxene (~–8 ‰), and plagioclase (–8 ‰ to –5 ‰), while $\Delta^{17}O$ increases from –5 ‰ to –3.5 ‰. Similar mass-independent fractionation of oxygen isotopes is found in the glassy ARC NWA 8649_A1, which shows ^{16}O-enrichment at the center ($\delta^{18}O$: –5 ‰; $\Delta^{17}O$: –4 ‰) compared to the other analyses towards the edge ($\delta^{18}O$: –1 ‰; $\Delta^{17}O$: –1 ‰). The remaining four glassy chondrules display internal oxygen isotope homogeneity with $\delta^{18}O$ and $\Delta^{17}O$ ranging from –9 ‰ to –1 ‰ and –4 ‰ to –1 ‰, respectively. Two analyses on the mottled region of glassy mesostasis in NWA 8276_A2 show $\delta^{18}O$ and $\Delta^{17}O$ of ~+5 ‰ and ~+1 ‰, respectively, significantly more positive that coexisting olivine and clean glass (Table 3). All analyses are plotted above the primitive chondrule mineral (PCM) and on/below the terrestrial fractionation (TF) line (Fig. 6).

3.5 Al-Mg isotopes

A total of 15 Al-Mg isotope analyses on olivine (N = 2), spinel (N = 3), and plagioclase (N = 10, three were rejected) from MET 00526_A2 were conducted (Table 4, Table S7-S9). The 12 valid analyses define an isochron (MSWD = 1.6) with an inferred $(^{26}Al/^{27}Al)_0$ of $(6.3 \pm 1.2) \times 10^{-6}$ and a

$\delta^{26}Mg^*_0$ of –0.08 ± 0.07 ‰ (Fig. 7). Slightly negative initial $\delta^{26}Mg^*_0$ is caused by the spinel analyses that do not show ^{26}Mg excess (~0 ‰) beyond the analytical uncertainty (2SE) of 0.15 ‰. The regression line excluding spinel show an inferred $(^{26}Al/^{27}Al)_0$ of (6.2 ± 1.2) × 10^{-6} and a $\delta^{26}Mg^*_0$ of 0.02 ± 0.10 ‰ (MSWD = 1.0), where spinel data overlap within their analytical uncertainties. The isochron using all data corresponds to a formation age of 2.15 ± $^{0.22}/_{0.18}$ Ma after CAI, under the assumption of a homogeneous distribution of ^{26}Al with a canonical value of 5.25 × 10^{-5} in the early solar system (Jacobsen et al., 2008; Larsen et al., 2011).

4. Discussion

4.1 Classification of OC ARCs

Petrologic classification of OC ARCs is challenging because most (~90 %) are dominated by glassy mesostasis indicative of rapid cooling that does not follow the phase equilibria. Based on their phenocryst types, Krot and Rubin (1994) divided glassy ARCs as glass/cryptocrystalline (90-99 vol% isotropic glass with skeletal crystals of olivine and high-Ca pyroxene), barred-olivine (BO), porphyritic olivine (PO), porphyritic pyroxene (PP), and porphyritic olivine-pyroxene (POP), in resemblance to the classification scheme of FMCs. The OC ARCs studied by Ebert and Bischoff (2016) and Ebert et al. (2022) are all glassy and were grouped as BO, PO, POP, and PP. Following this classification, NWA 8276_A2 of this study is PO, NWA 8276_A1 is BO, and MET 00526_A1 is POP. NWA 7731_A1 and NWA 8649_A1 are better classified as nonporphyritic because their high-Ca pyroxene is dendritic and significant Al-rich, comparable to the metastable high-Ca pyroxene in the run products of a CMAS melt (12.2 wt% CaO, 28.5 wt% MgO, 12 wt% Al_2O_3, and 47.3 wt% SiO_2) that crystallized under high degree of undercooling (olivine is the liquidus phase; Faure and Tissandier, 2014). Thus, the dendritic high-Ca pyroxene is a metastable phase rather than phenocrysts. The wide occurrence of skeletal olivine in these glassy ARCs also indicates a high degree of undercooling (Faure et al., 2003). Furthermore, the higher portion of glassy chondrules among OC ARCs compared to type I FMCs could be explained by their lower liquidus temperatures (~1400-1600 ℃ vs. ~1600-1800 ℃) (Hewins and Radomsky, 1990), where undercooling of

chondrule melts can be more easily achieved under similar cooling environments. For the barred-olivine texture in NWA 8276_A1, it implies either a fast-cooling (100-7200 K/h; Hewins and Radomsky, 1990; Lofgren and Lanier, 1990; Tsuchiyama et al., 2004) followed by multiple reheating steps or a slow-cooling of chondrule melt (<10 K/h; Faure et al., 2022).

The less common (~10 %) non-glassy ARCs are composed of well-crystallized plagioclase and high-Ca pyroxene with/without spinel, olivine, and low-Ca pyroxene. MacPherson and Huss (2005) studied eight non-glassy ARCs and divided them into two groups, i.e., porphyritic olivine (PO, N = 6) and porphyritic plagioclase (N = 2), basing on their bulk compositions and phase equilibria. Among the PO ARCs, three (Chainpur 1251-16-2, Chainpur 5674-3b-1, and Krymka 1729-9-1) have only 3-6 wt% bulk Al_2O_3 and should not be considered as ARCs. The remaining three have abundant olivine (Semarkona 4128-3-2 and Chainpur 1251-14-1, 38-46 wt%) or both olivine and low-Ca pyroxene (Quinyambie 6076-5-2, 30 wt% olivine, 37 wt% low-Ca pyroxene) phenocrysts, which are better named as PO and POP ARCs, respectively. For the two porphyritic plagioclase ARCs (Chainpur 5674-2-1 and Chainpur 1251-14-2), they are dominated by plagioclase laths and anhedral high-Ca pyroxene, with much lower olivine abundances than PO ARCs (0-15 wt% vs. 38-46 wt%). MET 00526_A2 of this study has mineral assemblage (spinel, olivine, plagioclase, and high-Ca pyroxene) almost identical to the two PO ARCs, but with a lower olivine abundance (~20 wt% olivine) that transits to porphyritic plagioclase ARCs. Thus, we conclude that the glassy and non-glassy ARCs share the same phenocryst types, and the key difference is their mesostasis types (glass vs. crystallized plagioclase + high Ca pyroxene), which primarily reflects their differences in cooling rate below the glass transition temperature (Tg, the transition from a viscous state to a brittle state) (Tronche et al., 2007; Wick and Jones, 2012) as well as the degree of undercooling as discussed above. For simplicity, we classify OC ARCs as glassy and plagioclase-bearing subtypes.

4. 2 Gas-melt interactions

It is widely accepted that chondrule formation occurred in open systems where interactions between chondrule melt and ambient gas have major effects on the petrologic, chemical, and

isotopic characteristics of the final products. Direct petrologic evidence for gas-melt interactions during chondrule formation include (i) mineralogically-zoned chondrules common in carbonaceous and ordinary chondrites, which have been reproduced by exposing chondrule-like melt to a gas of high SiO partial pressure in isothermal condensation experiments, indicating that the peripheral low-Ca pyroxene layer could have been formed by reactions between SiO gas and olivine crystals (Tissandier et al., 2002; Friend et al., 2016; Barosch et al., 2019); (ii) the near-equilibrium epitaxial growth of magnesium-rich olivine revealed by high-resolution CL images, suggesting that the condensation of gaseous Mg and SiO onto the chondrule melt supplied the growth of olivine crystals (Libourel and Portail, 2018; Marrocchi et al., 2018, 2019; Piralla et al., 2021); and (iii) concentric chemical zonation (MgO, SiO_2, Al_2O_3, TiO_2, etc.) across chondrule mesostasis, implying condensation of Mg, Si, Fe, and alkali elements during chondrule formation (Nagahara et al., 2008).

4.2.1 Major & trace element evidence for gas-melt interactions

Concentric chemical zonation of major elements across the glassy mesostasis was observed in NWA 8276_A2 of this study, with patterns broadly similar to those in the glassy ARC CH5 from Semarkona (Nagahara et al., 2008). Since olivine crystals are mostly located at the chondrule periphery, the crystallization of olivine would consume MgO, SiO_2, and FeO and enrich SiO_2 (bulk melt is richer in SiO_2 than olivine, ~47 wt% vs. ~43 wt%) and other incompatible elements (Al, Ti, Ca, V, Cr, Mn, Na, and K) in nearby melt (Kennedy et al., 1993; Libourel, 1999), resulting in monotonic decreases in MgO and FeO and increases of SiO_2, Al_2O_3, TiO_2, and CaO from the chondrule center to the surface. Meanwhile, positive correlations between incompatible elements and SiO_2 and flat correlations between other incompatible elements and Al_2O_3 would be established. However, the TiO_2 content is gradually decreasing toward the chondrule margin (Fig. 2e) and negatively correlated with SiO_2 content (Fig. 8d). Furthermore, the Al_2O_3 content does not exhibit a chondrule-scale zonation that increases outward (flat in the upper part and symmetric zonation in the lower part, Fig. 2e) and shows both positive and negative correlations with SiO_2 content (Fig. 8c). Since Al and Ti are both refractory elements (50% T_c >1582 K) (Lodders, 2003), these two observations indicate the continuous condensation of gaseous SiO onto the chondrule melt surface during olivine

458 crystallization, which diluted the concentrations of refractory elements of Al and Ti, as proposed by
459 Nagahara et al. (2008).

460 Contrary to outcomes of olivine crystallization at the surface, FeO content increases outward
461 (Fig. 2f) and shows a positive correlation with SiO_2 as well as the refractory element Al_2O_3 (Figs. 8b,
462 g), demonstrating the condensation of gaseous Fe onto chondrule melt during crystallization.
463 Diffusion of Fe from the chondrite matrix to the chondrule mesostasis during thermal metasomatism
464 is not adequate to establish this correlation between Fe and Si & Al because their diffusion rates in
465 silicate melts are different (Zhang et al., 2010). Furthermore, the MgO content, which is negatively
466 correlated with SiO_2 that follows the crystallization of olivine, displays both negative and positive
467 correlations with Al_2O_3, supporting that gaseous Mg was also condensed from ambient gas onto the
468 chondrule melt. This result is consistent with the condensation of gaseous SiO and Fe inferred
469 above because of their similar condensation temperatures (50% Tc ~1310-1336 K; Lodders, 2003).
470 The discontinuous layer of olivine at the surface of chondrules MET 00526_A2 (Fig. 1b), MET
471 00526_A1 (Fig. 1e), and NWA 8276_A2 (Fig. 2c), which is in contrast with the skeletal olivine grains
472 in the chondrules' interior, could also be resulted from condensation of gaseous Mg and SiO onto
473 chondrule melt that induced the crystallization of olivine at the surface (Nagahara et al., 2008;
474 Libourel and Portail, 2018). Minor elements V, Cr, and Mn display weak symmetric zonation across
475 the upper mesostasis of NWA 8276_A2 (Fig. S1), which can be explained by olivine crystallization at
476 the chondrule center and upper margin. Furthermore, they do not show positive correlations with the
477 refractory oxide Al_2O_3 (Fig. S2), arguing against the condensation of gaseous V, Cr, and Mn onto
478 chondrule melts, though their 50 % T_c of Cr and Mn are lower than Mg and SiO (<1300 K; Lodders,
479 2003). The nearly absent of condensation of V, Cr, and Mn gaseous species onto the chondrule
480 melts is interpreted to result from their low partial pressures in the ambient gas.

481 Glassy mesostasis in NWA 7731_A1 shows localized symmetric zonation of MgO, Al_2O_3,
482 SiO_2, and TiO_2 between dendritic high-Ca pyroxene bars (segments I, II, and IV), which could be
483 well explained by the crystallization of high-Ca pyroxene that consumed CaO, MgO, SiO_2, Al_2O_3,
484 TiO_2, and FeO, and concentrated Na_2O, SiO_2, Al_2O_3, and FeO (Fig. 3e) in the adjacent melt (bulk

melt is richer in SiO_2, Al_2O_3, and FeO than high-Ca pyroxene, ~50 wt% vs. 45 wt%, ~19 wt% vs. 15 wt%, and 0.11 wt% vs. 0.15 wt%, respectively) (Jones and Layne, 1997). Negative correlations between MgO and TiO_2 vs. SiO_2 and positive correlations between Al_2O_3 and FeO vs. SiO_2, as well as FeO and Na_2O vs. Al_2O_3 support this conclusion (Fig. 8). The Na_2O and FeO contents display chondrule-scale zonation that increases outward from the center (Fig. 3f), which haven't been disturbed by the crystallization of high-Ca pyroxene. The zonation profiles are concentric, with the peripheric ~100 μm layer being significantly richer in Na_2O compared to its interior and no significant Na-enrichments (small spikes) near interior cracks (Fig. 3d), indicating the condensation of gaseous Na and Fe onto the chondrule surface during crystallization. There is no clear evidence for gaseous Mg and SiO condensation onto the chondrule melt from the elemental distributions and correlations, while they must have condensed too because of their similar 50% T_c to Fe (Lodders, 2003). The lack of such evidence could be due to the overprint of the crystallization effects of high-Ca pyroxene onto the condensation effects of Mg and SiO, where high-Ca pyroxene crystallized as a metastable phase from a highly undercooled melt (Faure and Tissandier, 2014). This overprint process occurred at a lower temperature, under which the condensation of most gaseous species (like Mg, SiO, and Fe) ceased, different from the case of NWA 8276_A2 that olivine crystallization and gaseous condensation occurred contemporarily. The crystallization of high-Ca pyroxene disturbed the distributions of MgO and SiO_2 established by condensation, but weakly affected those for Na_2O and FeO, because the latter two are minor elements in high-Ca pyroxene.

4.2.2 Oxygen isotope evidence for gas-melt interactions

The plagioclase-bearing ARC MET 00526_A2 shows $\delta^{18}O$ heterogeneity with early-crystallized spinel (~–10 ‰) and olivine (~–9 ‰) being more negative compared to late-crystallized high-Ca pyroxene (~–8 ‰) and plagioclase (~–8 ‰ to –5 ‰) (Fig. 6), while their $\Delta^{17}O$ values are within a small range of ~–5 ‰ to ~–3.5 ‰. Multiple analyses on spinel, olivine, and high-Ca pyroxene grains show almost identical $\delta^{18}O$ values, suggesting that this heterogeneity is not related to relict phases. The more variable and ^{16}O-depleted signatures of plagioclase could be due to continuous exchange with ambient gas during its prolonged crystallization under a cooling rate of

512 1°C/hr in the range of 1000°C to 800°C (Wick and Jones, 2012) or with fluid during asteroidal
513 metasomatism as suggested by the common occurrence of scapolite (Fig. 1c). For spinel, olivine,
514 and high-Ca pyroxene that having sluggish oxygen isotope self-diffusion rates (Houlier et al., 1988;
515 Ryerson and McKeegan, 1994), they show <1 ‰ variability in $\Delta^{17}O$ (not clearly resolved) and ~2 ‰
516 variability in $\delta^{18}O$. Their $\delta^{18}O$ and $\delta^{17}O$ are distributed along a slope ~0.94 line, suggesting that this
517 $\delta^{18}O$ heterogeneity is mainly mass-independent instead of being mass-dependent relating to
518 chondrule melt evaporation (Kita et al., 2010; Piralla et al., 2021). If plagioclase is included in the
519 regression, the slope becomes ~0.87, clearly differing from the slope ~0.52 mass-dependent
520 fractionation line. Thus, we consider that the apparent correlation between $\delta^{18}O$ values and the
521 mineral crystallization sequence was most likely established by oxygen isotope exchange between
522 chondrule melt and ambient gas during its crystallization. Similarly, three analyses on the glassy
523 mesostasis of NWA 8649_A1 show $\Delta^{17}O$ from –4 ‰ to –1 ‰, with $\delta^{18}O$ and $\delta^{17}O$ distributing along a
524 slope ~1 line over a range of ~5 ‰ (Fig. 6). Assuming the glassy mesostasis in NWA 8649_A1 and
525 those in FMCs from LL3.0-3.1 chondrites were exchanged by the same fluid, the regression slope
526 derived from the former would be shallower than ~0.8 derived from the latter (Kita et al., 2010),
527 which is not the case for NWA 8649_A1. Furthermore, the center analysis is more ^{16}O-enriched than
528 the peripheral ones. These observations suggest that this heterogeneity is most likely the state of
529 the gas-melt exchange process frozen by the rapid cooling of this small droplet (~200 μm). If it is true,
530 this chondrule melt must have remained molten for a very short period because the oxygen isotope
531 homogenization timescale for a ~200 μm basaltic droplet at 1450 ℃ is ~0.4 hours (Lesher et al.,
532 1996). Moreover, it is also possible that the plagioclase of MET 00526_A2 and glassy mesostasis of
533 NWA 8649_A1 experienced partial oxygen isotope exchange with fluids during asteroidal
534 metasomatism and resulted in their internal $\delta^{18}O$ heterogeneity (see section 4.3.1).

535 The dependence of ^{16}O enrichment on the degree of melting (porphyritic ones are richer in
536 ^{16}O than nonporphyritic ones) found in ARCs by Russell et al. (2000) is inconsistent with the
537 observations of this study. The nonporphyritic ARCs NWA 7731_A1 ($\Delta^{17}O$: –3.6 ‰) and NWA
538 8649_A1 ($\Delta^{17}O$: –4 ‰ to –1 ‰) are more ^{16}O-enriched than the BO ARC NWA 8276_A1 ($\Delta^{17}O$: –

539 0.8 ‰) and the PO ARC NWA 8276_A2 ($\Delta^{17}O$: –0.3 ‰), but like the POP ARC MET 00526_A1
540 ($\Delta^{17}O$~ –3 ‰). Instead, we believe that the oxygen isotope ratios of ARCs are highly dependent on
541 the degree of oxygen isotope exchange with ^{16}O-poor ambient gas in addition to their precursors
542 (initial melts).

543 **4.3 Parent body processes of OC ARCs**

544 4.3.1 Aqueous alteration

545 Contrary to the conventional view of dry conditions, evidence of aqueous alteration has been
546 primarily found in the most primitive OC chondrite Semarkona (LL3.00), including the presence of
547 phyllosilicates and carbonates in chondrule mesostasis and inter-chondrule matrix (Hutchison et al.,
548 1987; Alexander et al., 1989, 2015; Grossman and Brearley, 2005), “bleached chondrules”
549 (mesostasis in their outer portions have been bleached and left a porous zone depleted in alkalis
550 and Al) (Grossman et al., 2000), carbide-magnetite assemblages (Krot et al., 1997), “zoned
551 chondrules” (“sub-parallel” zonation profiles of moderately volatile elements and Ca in their
552 mesostasis) (Grossman et al., 2002), oxidized iron and iron-rich olivine in matrix and/or
553 microchondrules (Dobrică et al., 2019; Dobrică and Brearley, 2021), and disturbed Na and Ca
554 zonation in plagioclase (Lewis and Jones, 2019).

555 Aqueous alteration features have also been identified among the six ARCs of this study,
556 which are from OCs with low petrologic types (3.05) slightly more metamorphosed than Semarkona
557 (Siron et al., 2022). The occurrence of scapolite within the mesostasis, along the boundaries of
558 phenocrysts, and especially at the lower center of the plagioclase-bearing ARC MET 00526_A2 (Fig.
559 1c) suggests that it is a secondary product of plagioclase via aqueous alteration, where Na_2O, K_2O,
560 Cl, and FeO were introduced, and CaO was leached out. An LA-ICP-MS analysis on the scapolite-
561 rich region shows a significant depletion of RLEs with strong enrichments of Sr, Ba, and Eu (Fig. 5d),
562 supporting the hypothesis that its parental phase was plagioclase. Furthermore, the hydrated portion
563 (Fig. 2) of NWA 8276_A2 is depleted in Na_2O, CaO, and Al_2O_3 and enriched in FeO, NiO, and K_2O
564 compared to interior clean glassy mesostasis, which is similar to the bleached chondrules described

565 by Grossman et al. (2000). Its interior mesostasis shows complementary and irregular profiles of
566 Na_2O and CaO (Fig. 2f) and a wide concentration range of Rb (0-4 × CI; Fig. 5b), suggesting that
567 CaO was replaced by Na_2O and the initial distributions of Na_2O and Rb were disturbed by aqueous
568 alteration. Meanwhile, the distributions of Al_2O_3, MgO, SiO_2, TiO_2, and FeO established by olivine
569 crystallization and gas-melt interactions remain largely intact because of their possible slower
570 diffusion rates in silicate glasses assuming their relative diffusivities are comparable to those in
571 silicate melts (Zhang et al., 2010). The oxygen isotope ratios obtained from its mottled mesostasis
572 are significantly enriched in ^{18}O and ^{17}O compared to clean regions (~4 ‰ vs. 0 ‰ and ~3 ‰ vs.
573 0 ‰, respectively; $\Delta^{17}O$: +0.6‰ vs. –0.3‰; Table 3), supporting that a fluid with heavy oxygen
574 isotopes has altered its composition.

575 4.3.2 Implication for Na-Al-rich chondrules in metamorphosed OCs

576 In metamorphosed OCs, thermal metamorphism was found to be assisted by fluid that
577 resulted in the formation of nepheline, sodalite, scapolite, amphibole, carbide-magnetite
578 assemblages, phosphate, and K-feldspar (Rubin and Grossman, 1985; Bridges et al., 1997; Krot et
579 al., 1997; Russell et al., 2000; Dobrică and Brearley, 2014; Jones et al., 2014; Lewis et al., 2022).
580 Plagioclase is weakly resistant to fluid alteration and could be replaced by sodalite/scapolite in types
581 3.2-3.6, nepheline in types 3.4-3.9, and albite in types 3.6-5 OCs (Lewis et al., 2022). Therefore,
582 previous studies on ARCs from metamorphosed type 3.1-4 OCs found plagioclases mostly altered to
583 nepheline; however, glassy mesostasis, which is more easily altered by fluids than plagioclase, was
584 found to be abundant and enriched in Na-Al (Bischoff and Keil, 1984; Krot and Rubin, 1994; Russell
585 et al., 2000; MacPherson and Huss, 2005; Jiang et al., 2015; Ebert and Bischoff, 2016; Varela and
586 Zinner, 2018; Ebert et al., 2022).

587 The Na-Al-rich chondrules are thought to have formed by remelting mixtures of a refractory
588 CAI/AOA-like component and a nepheline-rich component in closed systems with high Na partial
589 pressure (Bischoff and Keil, 1984; Krot and Rubin, 1994; Ebert and Bischoff, 2016). This hypothesis
590 is inconsistent with the open system behaviors evidenced by major element distributions and

591 correlations and oxygen isotope signatures of ARCs in Semarkona (Nagahara et al., 2008) and OCs
592 of this study (section 4.2). It also contradicts with interpretations of post-olivine crystallization entry of
593 Na into chondrule melt as suggested by the high precision EPMA analyses of sodium in olivines of
594 Na-Al-rich chondrules (Ebert et al., 2022). Instead, we argue that they are most likely
595 metamorphosed Ca-Al-rich chondrules since (i) the two have almost identical textures and mineral
596 assemblages (glassy mesostasis with dendritic high-Ca pyroxene and skeletal olivine); (ii) the
597 relative abundance of the two correlates with the petrologic type of host meteorites, with the former
598 (Na-Al-rich) being almost absent in pristine OCs (3.05, this study), coexisting with the latter in mildly
599 metamorphosed OCs (3.1-3.2; Ebert et al., 2022), and dominating in moderately metamorphosed
600 (3.3-4) OCs; (iii) the compositional differences between the two can be explained by substitutions of
601 Na and K for Ca and of Fe for Mg during thermal metamorphism (Huss et al., 2006), i.e., the glassy
602 mesostasis in the former are significantly richer in Na_2O (4-16 wt% vs. <1 wt%), K_2O (<2.5 wt% vs.
603 ~0 wt%), FeO (0.7-5.6 wt% vs. <0.5 wt%) and poorer in CaO (0-15 wt% vs. 15-20 wt%) and MgO (0-
604 11 wt% vs. 4-11 wt%), and the phenocrysts (spinel, olivine, and low-Ca pyroxene) are iron-rich (up
605 to 32 wt%) (Krot and Rubin, 1994; MacPherson and Huss, 2005; Jiang et al., 2015; Ebert and
606 Bischoff, 2016; Ebert et al., 2022), compared to the latter; and (iv) the majority of mesostasis in the
607 former are significantly ^{16}O-depleted (Ebert et al., 2022), while those in the latter are mostly not, as
608 compared to their coexisting phenocrysts, suggesting that the oxygen isotope signatures in the
609 former were modified by asteroidal fluids.

610 While abundant evidence exists for transforming Ca-Al-rich chondrules to Na-Al-rich
611 chondrules by asteroidal metasomatism, here are three major difficulties in understanding how these
612 textures have been preserved. First, how to prevent glassy mesostasis from bleaching during
613 aqueous alteration? This can be explained by the low water-rock ratio of the OC parent bodies (e.g.,
614 Alexander et al., 1989), where the metasomatism effects were subtle and localized. Previous studies
615 on Semarkona chondrules found mainly the outer zones of radial pyroxene and cryptocrystalline
616 chondrules were severely bleached (Grossman et al., 2000), while the porphyritic chondrules were
617 bleached randomly to varying degrees (Lewis and Jones, 2019). Furthermore, metasomatism

618 products of Na-/Cl-rich phase (Na-Cl-rich glass, nepheline, sodalite, and scapolite) were identified in
619 only ~7-8 % chondrules in metamorphosed OCs Chainpur (LL3.4) and Parnallee (LL3.6) (Bridges et
620 al., 1997).

621 Second, how to preserve the glassy mesostasis of OC ARCs from devitrification during
622 progressive thermal metamorphism? It is known that isotropic glass is less common in chondrules
623 from OC>3.4 meteorites (metamorphic temperature >400-600°C) (Huss et al., 2006), but the glassy
624 mesostasis in ARCs from type 3-4 OCs remains mostly vitreous with minor peripheral zones being
625 devitrified (Krot and Rubin, 1994; MacPherson and Huss, 2005; Jiang et al., 2015; Ebert and
626 Bischoff, 2016). We attribute the survival of glassy mesostasis in ARCs to their Ca-Al-rich
627 compositions, where the Tg of a calcium aluminosilicate glass with similar composition (Al/Ca ratio
628 ~1, SiO_2 ~50 wt%) is ~800°C (Shelby, 1985). This Tg, while it is pressure-dependent, is significantly
629 higher than the peak metamorphic temperature (400-600 °C) of type 3-4 OCs but lower than that of
630 type 4-6 OCs (≤950 °C), matching well with the absence of glassy ARCs in OCs with petrologic
631 type >4 (Krot and Rubin, 1994; MacPherson and Huss, 2005; Jiang et al., 2015; Ebert and Bischoff,
632 2016).

633 Third, what are the sources of sodium in Na-Al-rich chondrules? It is known that sodium
634 could be leached from the mesostasis and plagioclase of ARCs and FMCs by low-pH fluids at the
635 earliest stage of thermal metamorphism (petrologic type ≤3.1) (Grossman et al., 2000; Lewis et al.,
636 2022), resulting in the elevation of pH in the fluids that contributed to the formation of feldspathoids
637 (mainly nepheline) during prograde thermal metamorphism (petrologic type 3.1-3.9) (Lewis et al.,
638 2022). At this stage, the highly mobile Na in the fluids could have been reincorporated by the ARCs,
639 either by pooling in the bleached glass or substituting Ca in unbleached ones, followed by
640 dehydration due to the loss of the fluid on the asteroid through peak metamorphism. The high
641 normative albite + nepheline compositions for the mesostasis of Na-Al-rich chondrules (Ebert and
642 Bischoff, 2016), as well as the occurrence of Ca-rich rim around a Na-Al-rich chondrule (Ebert et al.,
643 2022), are consistent with the hypothesis that they were formed by bleaching Ca-Al-rich chondrules
644 followed by feldspathoid crystallization and dehydration during prograde thermal metamorphism.

4.4 Precursors of OC ARCs

4.4.1 Implications from bulk major element abundances

Bulk compositions of OC ARCs are significantly enriched in Al_2O_3, TiO_2, and CaO compared to FMCs (Fig. 9a), explicitly suggesting a refractory component in their precursors. On the ternary diagram of Ca_2SiO_4–Mg_2SiO_4–Al_2O_3 projected from spinel (Fig. 10), the OC ARCs of this study are richer in MgO and poorer in CaO compared to the pyroxene-anorthite-rich CAIs (igneous type C CAIs in CVs and condensate CAIs in COs and Acfer 094) and fine-grained spinel-rich CAIs. This implies that the two types of CAIs could be among their precursors, but simply remelting them couldn't produce OC ARCs; therefore, a nonrefractory source is needed. Because OC ARCs are Fe-poor with minor or free of Fe-Ni metals and iron sulfides, the nonrefractory component could either be (i) the precursor of type I chondrules ("CAI-FMC hybrids," MacPherson and Huss, 2005); or (ii) the ambient gas, i.e., gaseous Mg and SiO condensed onto the CAI melts and modified their bulk compositions ("CAI-Gas model"; Nagahara et al., 2008). Along with four Semarkona and three NWA 7402 (LL3.1) ARCs from the literature (Rubin, 2004; MacPherson and Huss, 2005; Nagahara et al., 2008; Ross et al., 2017), the ARCs from OCs with petrologic type <3.1 are distributed along the anorthite-forsterite join toward the forsterite apex of the ternary diagram (Fig. 10), rather than extending from the two types of CAIs to type I chondrules, supporting that "CAI-Gas" model. On the diagram of SiO_2–CaO+Al_2O_3–MgO (Fig. 10 of Nagahara et al., 2008), these OC ARCs follow a nearly linear trend that intersects the MgO-SiO_2 axis at an atomic ratio of 3:2 to 2:1 (forsterite, Fig. S4), indicating that the gaseous Mg and SiO added to the chondrule melt was at an atomic ratio of ~3:2 to ~2:1. Furthermore, the bulk compositions of metamorphosed OC ARCs, corrected for the Fe-Mg and (Na, K)-Ca exchanges due to thermal metasomatism, overlap largely with pyroxene-anorthite-rich CAIs and partially with fine-grained spinel-rich CAIs (Fig. 10). Like those from OCs with petrologic type <3.1, their bulk compositions are well-distributed along the An-Fo join, as illustrated by their 2D Kernel density distributions of the three apexes (Forsterite, Corundum, and Larnite) calculated from their corrected bulk compositions (Fig. S3).

671 4.4.2 Implications from bulk trace element abundances

672 Bulk RLE (Zr, Hf, Sc, Y, Ti, Sr, Ba, and REEs, ~7-15 × CI) abundances of OC ARCs in this
673 study are significantly enriched compared to FMCs (1-3 × CI for Sc, Hf, La, Sm, Eu, Tb, Yb, and Lu,
674 determined by INNA) (Gooding et al., 1980; Grossman and Wasson, 1982, 1983; Kurat et al., 1984;
675 Rubin and Pernicka, 1989; Swindle et al., 1991), suggesting a refractory RLE-rich component in their
676 precursors, most likely CAIs (tens of CI, e.g., Grossman, 1973; Mason and Martin, 1977; Mason and
677 Taylor, 1982). The findings of group II (occasionally with negative Sm anomaly) and III REE patterns
678 in five out of nine OC ARCs (Fig. 5e) studied by Ebert and Bischoff (2016), which were established
679 during condensation from a gas of near solar composition in the earliest epoch of the protoplanetary
680 disk (Boynton, 1975; Davis and Grossman, 1979), undoubtedly indicate that the refractory
681 component is CAIs. The OC ARCs of this study all display unfractionated (group I, Fig. 5a-d) REE
682 patterns similar to those reported in MacPherson and Huss (2005), suggesting that RLEs in the
683 majority of OC ARCs (17 out of 22) are unfractionated, in stark contrast with ARCs in CV chondrites
684 (7 out of 11 have fractionated group II/-like or III REE patterns; Wakaki et al., 2013; Zhang et al.,
685 2014; Zhang et al., 2020b). This observation rules out the possibility of fine-grained spinel-rich CAIs,
686 which typically have fractionated group II REE patterns (e.g., Krot et al., 2004b), as the refractory
687 component in the precursors of OC ARCs.

688 Bulk Cr and Mn abundances of OC ARCs in this study are depleted to varying degrees (Cr =
689 0.2-0.6 × CI, Mn = 0.1-0.4 × CI, Figs. 5) compared to OC FMCs (~1-3 × CI) (Gooding et al., 1980;
690 Grossman and Wasson, 1982, 1983; Kurat et al., 1984; Rubin and Pernicka, 1989; Swindle et al.,
691 1991). In section 4.2.1, elemental distribution and intercorrelations demonstrated that almost no
692 recondensation of Cr and Mn occurred during melt crystallization. Thus, the depletion of Cr and Mn
693 in OC ARCs indicates a Cr-Mn-depleted component in their precursors, most likely CAIs (Cr<0.7 ×
694 CI and Mn<0.5 × CI; Grossman, 1973; Grossman and Ganapathy, 1975; Grossman and Ganapathy,
695 1976b, a; Sylvester et al., 1993).

696 Since REE-unfractionated CAIs and OC FMCs both exhibit limited ranges of REE
697 abundances (~18 ± 4 × CI in CAIs and 1.8 ± 1 × CI in FMCs) (Martin and Mason, 1974; Wänke et al.,

1974; Mason and Martin, 1977; Gooding et al., 1980; Grossman and Wasson, 1982, 1983; Mason and Taylor, 1982; Kurat et al., 1984; Rubin and Pernicka, 1989; Swindle et al., 1991; Sylvester et al., 1993; Huang et al., 2012; Davis et al., 2018; Torrano et al., 2019, 2023), it is possible to estimate the portion of CAI component in the precursors of OC ARCs based on their REE abundances. Rough calculations suggest that the CAI component accounts for ~30-100 % of their precursors (Table 2, Fig. 9b); the wide range is due to the relatively large uncertainty of REE abundance of the CAI endmember. Applying the same calculation to REE-unfractionated OC ARCs in the literature (Chainpur 5674-2-1 & 1251-14-2 & 1251-3-1, Inman 5652-1-1, and Hammadah al Hamdra 335-3) (MacPherson and Huss, 2005; Ebert and Bischoff, 2016) indicate a portion of CAI of ~30-100 %. Furthermore, the REE abundances of Semarkona 4128-3-2, Chainpur 1251-14-1, Quinyambie 6076-5-2, and Hammadah al Hamdra 335-1 (MacPherson and Huss, 2005; Ebert and Bischoff, 2016) are too low to suggest a CAI component in their precursors.

Utilizing the CAI portion estimated from REEs and the average compositions of type IA and IAB/IB chondrules ("CAI-FMC hybrid" model; Jones and Scott, 1989; Jones, 1994) or the inferred ambient gas composition (MgO:SiO~3:2 to 2:1; Nagahara et al., 2008), the major element compositions of the CAIs incorporated into the precursors of OC ARCs are roughly calculated to contain 15-25 wt% CaO, 15-35 wt% Al_2O_3, 0-20 wt% MgO, and 30-50 wt% SiO_2 (assume similar gaseous recondensation effects for OC ARCs and type I chondrules; “CAI-FMC hybrid” model) or 15-25 wt% CaO, 20-35 wt% Al_2O_3, 0-15 wt% MgO, and 30-50 wt% SiO_2 (the “CAI-Gas” model). The inferred composition ranges are very similar, and both significantly overlap with pyroxene-anorthite-rich CAIs on the ternary diagram of Ca_2SiO_4–Mg_2SiO_4–Al_2O_3 (green and magenta zones in the inset of Fig. 10), making this type of CAI to be the best candidate recycled by OC ARCs. Furthermore, to avoid negative MgO and SiO_2 contents for the CAI component, the lower limit portion of the CAI component is typically higher than that estimated from REE abundances (Table 2). It is noteworthy that the bulk V content of OC ARCs of this study (0.3-1.9 × CI) and the literature (0.7-3.5 × CI; Ebert and Bischoff, 2016) are significantly lower than other RLEs (i.e., Zr, Hf, Sc, Y, Ti, Sr, Ba, and REEs,

~7-15 × CI), implying a significant loss of V via unknown processes associated with chondrule formation or asteroidal metamorphism.

4.4.3 Implications from oxygen isotopes

Previous studies found oxygen isotopes of OC ARCs extend from the typical oxygen isotope region of FMCs toward a more ^{16}O-enriched endmember ($\delta^{18}O$ down to –15 ‰) along a line of slope 0.83 ± 0.09 (Russell et al., 2000) or 0.7 ± 0.1 (Jiang et al., 2015). The mixing lines are shallower than the carbonaceous chondrite anhydrous minerals line (CCAM, slope = 0.941, intercept = –4.00; Clayton et al., 1973) and the primitive chondrule minerals line (PCM, slope = 0.987, intercept = –2.70; Ushikubo et al., 2012) and do not intersect with the oxygen isotope region of CAIs, indicating that the OC ARCs are not simple mixtures of CAIs and FMC materials. In contrast, a recent study by Ebert et al. (2022) found that the oxygen isotopes of spinel, olivine, and low-Ca pyroxene in metamorphosed OC ARCs roughly follow the Young & Russell line (slope = 1.00, intercept = –1.044; Young and Russell, 1998) or the PCM line (Ushikubo et al., 2012), and argued that their precursors could be a mixture of CAIs(-like) and FMC materials. In this study, we determined oxygen isotope ratios of six ARCs from type 3.05 OCs with significantly improved analytical precision (~0.2-0.5 ‰ for $\delta^{18}O$) and found that they distribute along a mixing line of $\delta^{17}O = (0.99 \pm 0.05) \times \delta^{18}O - (0.40 \pm 0.32)$ (MSWD = 2.4, based on data in Table 3 excluding altered glass, Fig. 11, named “OC ARC line”). Semarkona ARC CH5 (Kita et al. 2010) is consistent with the OC ARC line and located near the intersection with the terrestrial fractionation line (TFL, Fig. 11a). Unlike CCAM and PCM lines, the mixing line is less well constrained (slope ranges from 0.92 to 1.04, orange shadowed region in Fig. 11), due to their small variations in oxygen isotopes (~10 ‰ in $\delta^{18}O$).

The OC ARC line plots on the left (lower $\delta^{18}O$) of most OC type IAB, IB, and II chondrules (Fig. 11a; except for IAB chondrules Bishnupur B12, Semarkona CH33, and NWA 7731 C5 that are on the OC ARC line; Kita et al. 2010; Siron et al., 2022), suggesting that the ^{16}O-poor endmember is not the precursor of these types of FMCs. In contrast, the OC ARC line intersects with type IA chondrules with $\Delta^{17}O$ >0‰ (“supra-TFL” group defined by Marrocchi et al., 2024), which displays

large mass-dependent isotope fractionations with $\delta^{18}O$ ranging from ~–3‰ to ~+9‰ (Fig. 11b). For type IA chondrules with $\Delta^{17}O$ <0‰ ("sub-TFL" group defined by Marrocchi et al., 2024), most are consistent with the PCM line that could have recorded the oxygen isotope evolving from ^{16}O-rich to ^{16}O-poor in the OC chondrule-forming regions (Kita et al., 2010; Marrocchi et al., 2024). The relict olivines ($\Delta^{17}O$ ~–5 ‰ to –2 ‰) identified in IA chondrules by Kita et al., (2010) and Piralla et al. (2021) are likely to be unmelted fragments of the pre-existing sub-TFL chondrules (Marrocchi et al., 2024). As exceptions, some sub-TFL IA chondrules plot on the OC ARC line and have either lower or higher $\delta^{18,17}O$ than OC ARCs of this study (Fig. 11b). Thus, as indicated by Nagahara et al. (2008), OC ARCs and some type IA chondrules could have formed from common refractory and ferromagnesian precursor solids and experienced open-system formation that involved evaporation and re-condensation of Mg and SiO.

Toward the lower end, the OC ARC line intersects with the typical oxygen isotope region of CAIs and AOAs on the CCAM and PCM lines (Fig. 11c), supporting the interpretation that CAIs were among the precursors of OC ARCs. The two AOA-like relict olivines ($\Delta^{17}O$ <–15 ‰) identified among eleven IA chondrules by Piralla et al. (2021) are consistent with the PCM line and, within uncertainty, also with the OC ARC line. The rarity of AOA-like olivines in OC FMCs suggests that AOAs and possibly CAIs existed but as a minor component in the OC chondrule-forming region. Considering the large portion of CAIs in their precursors (30-90%), the OC ARCs seem to be less ^{16}O-enriched, as noticed by Russell et al. (2000), which could be due to the extensive gas-melt interactions that significantly diluted the initial oxygen isotope ratios of the chondrule melt.

4.4.4 The Ti isotope conundrum

The involvement of CAIs in the formation of OC ARCs seems to conflict with the Ti isotope signatures of Na-Al-rich chondrules from metamorphosed OCs, which are indistinguishable from OC FMCs ($\varepsilon^{50}Ti$ ~0) and much lower than that of OC CAIs ($\varepsilon^{50}Ti$ ~2-11) and CO ARCs ($\varepsilon^{50}Ti$ ~2-15) (Ebert et al., 2018). Since Ti is an immobile element and no Ti gain/loss was observed in ARCs of this study (section 4.2.1), the Ti isotope signatures of OC ARCs suggest the existence of a refractory

776 component without ^{50}Ti excess in the inner solar system as proposed by Ebert et al. (2018).
777 Combined with our discussions above, the most possible refractory components for OC ARCs are
778 pyroxene-anorthite-rich CAIs, which likely formed by gas condensation at lower temperatures near
779 the protosun (~1300-1450K; Ebel and Grossman, 2000). The component could be indigenous in the
780 inner disk, which might have been trapped in a magnetically dead zone at the midplane of the
781 protoplanetary disk before the onset of chondrule formation (Jacquet et al., 2011), or exotic from the
782 outer disk by inward drifting through the Jupiter gap (Desch et al., 2018; Haugbølle et al., 2019). In
783 this study, MET 00526_A2 appears to show mass-independent oxygen isotope fractionation and has
784 an Al-Mg age of 2.15 ± $^{0.22}/_{0.18}$ Ma that is within the range of OC FMCs (~1.2-3.0 Ma; Fig. 12;
785 Hutcheon and Hutchison, 1989; Kita et al., 2000; Rudraswami and Goswami, 2007; Rudraswami et
786 al., 2008; Villeneuve et al., 2009; Mishra et al., 2010; Bollard et al., 2019; Pape et al., 2019; Siron et
787 al., 2021, 2022). If only the most recent Al-Mg data of OC FMCs were considered (~1.8-2.2 Ma;
788 Siron et al., 2021, 2022), various types of chondrules display a limited range of ~0.4 Ma and are
789 mostly indistinguishable to each other. While the inferred Al-Mg age of MET 00526_A2 overlaps with
790 the majority of FMCs studied by Siron et al., (2021, 2022) within analytical errors, data plot close to
791 the younger limit and postdate formation of a half of the anorthite-bearing chondrules occurring at
792 ~1.9 Ma (Fig. 12). Nevertheless, the internal oxygen isotope variation of MET 00526_A2 indicates
793 that it might not have been remelted/recycled after solidification (otherwise, homogenized). Thus, its
794 Al-Mg age indicates that the refractory component in its precursor must arrive at the OC regions
795 after, rather than before, the onset of the chondrule heating events.

796 It is worth noting that spinel of MET 00526_A2 does not show resolvable ^{26}Mg excess,
797 differing from the spinels in two OC FMCs (Semarkona ch10 and Piancaldoli ch8) that show large
798 excess that indicates an age of ~0.8 Ma (Piralla et al., 2023). Piralla et al., (2023) argued that Mg
799 diffusion in spinel is slower than in plagioclase, though Mg diffusion in plagioclase shows a strong
800 dependence to anorthite composition (Van Orman et al., 2014) and those for An ≥ 93 are slower
801 than that of spinel (Sheng et al., 1992; LaTorrette and Wasserburg, 1998; Van Orman et al., 2014).
802 Plagioclase in MET 00526_A2 are anorthitic (An_{91-99}) so that it is unlikely that spinel recorded earlier

803 formation age than the isochron determined by plagioclase data. More studies are required to
804 examine spinel Al-Mg chronology from chondrules in which plagioclase preserved correlated ^{26}Mg
805 excess.

806 To further reveal the characteristics of this refractory component, more high-precision Ti
807 isotope analyses on other non-carbonaceous materials, for example, the ARCs in enstatite
808 chondrites, are necessary to confirm the universal existence of this unique refractory material in the
809 inner protoplanetary disk. Meanwhile, to eliminate the concern of the effects of thermal
810 metamorphism on the preservation of primary Ti isotope signatures, self-diffusion experiments of Ti
811 isotopes in Ca-Al-silicate glass or direct measurements of ARCs in OCs with low petrologic types are
812 needed.

813 **4.5 Formation mechanism for OC ARCs**

814 To summarize the discussions above, we outline the formation mechanism for OC ARCs as
815 follows (Fig. 13): (i) Stage I: condensation of pyroxene-anorthite-rich CAIs from nebular gas between
816 1300-1450 K near the protosun. The CAIs are characterized by solar-like ^{16}O-rich signatures,
817 unfractionated and, in rare cases, fractionated REE abundances, and absence of ^{50}Ti excess. They
818 could have been produced indigenous and then preserved in a magnetically dead zone of the inner
819 disk or transported in from the outer disk by gas drag; (ii) Stage II: Flash melting of the CAIs
820 subsequently interacted extensively with the ambient gas in the chondrule-forming region. During
821 mineral crystallization, gaseous Mg, SiO, Fe, and alkalis condensed onto the melts, and meanwhile,
822 diluted the ^{16}O-rich signatures of the initial melt by the ^{16}O-poor gas and established the correlation
823 between ^{16}O-enrichments and mineral crystallization sequence for MET 00526_A2. The atomic ratio
824 of condensed MgO and SiO was inferred to be ~3:2 (Nagahara et al., 2008) to ~2:1; and (iii) Stage III:
825 Asteroidal modifications of the mineralogy and oxygen isotopes of OC ARCs by fluids, including
826 bleaching glassy mesostasis by low-T fluids, followed by replacement of glassy mesostasis and
827 plagioclase with feldspathoids and dehydration during prograde metamorphism, transforming Ca-Al-
828 rich chondrules into Na-Al-rich chondrules.

Bischoff et al., (1989) first proposed that OC ARCs could be splashed melts of partially molten FMCs because of their fractionated REE patterns. The splash model was argued against by Ebert and Bischoff (2016) since there are no systematic size differences between the two. Marrocchi et al., (2024) broaden the splash model from OC ARCs to sub-TFL IA chondrules, which appears to be smaller than supra-TFL IA and other types of chondrules. The six ARCs of this study show variable sizes (~1100 μm to ~200 μm) and modal mineral abundances (0-44 vol% olivine) that cannot be explained by the splash model. They show flat REE patterns (Fig. 5) without depletion in Mg (Fig. 9a, 0.8-2 ×CI), suggesting that they are not residual melts after the crystallization of olivine and/or pyroxene. Furthermore, their oxygen isotopes are distributed on a line distinct from the majority of OC FMCs (Fig. 11a, b), indicating that they formed from different precursors and exchanged with isotopically different ambient gases. Thus, we consider the splash model to be invalid for the formation of OC ARCs and possibly the sub-TFL IA chondrules studied by Marrocchi et al., (2024).

5. Conclusions

We characterized petrography, mineralogy, bulk major and trace element chemistry, and oxygen isotopes of six ARCs from OC3.05 meteorites. The plagioclase-bearing ARC was also investigated with Al-Mg chronology. The findings provide better understanding of the mechanisms of OC ARC formation, including their precursor compositions, gas-melt interactions, and asteroidal metasomatism. Key observations and their interpretations are listed below.

(1) Chondrule-scale chemical zonation of major elements (Mg, Si, Al, Ti, Fe, and Na) and their inter-element correlations in the glassy mesostasis of two ARCs demonstrated the condensation of gaseous Mg, SiO, Fe, and alkalis onto chondrule melts.

(2) Bulk major element compositions of ARCs from OC<3.1 meteorites are closest to the pyroxene-anorthite-rich CAIs and follow a nearly linear trend toward the Mg: SiO ~ 3:2 to 2:1 (in atomic) apex, suggesting that OC ARCs could be made by varying degrees of gaseous Mg and SiO condensation onto bulk melts of pyroxene-anorthite-rich CAIs. Their bulk trace element

concentrations display unfractionated REE patterns (~7-15 × CI) with varying depletions of V, Cr and Mn, indicating that 30-100 % of the bulk is contributed by CAIs.

(3) Oxygen isotopes of the plagioclase-bearing ARC, MET 0526_A2, show ^{16}O-rich enrichments following the mineral crystallization sequence, demonstrating gas-melt oxygen isotope exchange during crystallization. A similar case is NWA 8649_A1, which shows ~3 ‰ variation of Δ^{17}O in its glassy mesostasis. Together with the remaining three displaying oxygen isotope homogeneity, all OC ARCs of this study plot along a line of slope ~0.99 ± 0.05 that is almost parallel to the PCM line but towards higher δ^{17}O. The OC ARC mixing line intersects with the CAIs/AOAs, consistent with a small number of IA chondrules, but deviates from the majority of OC FMCs (IAB/IB/II), suggesting a possible genetic relationship between OC ARCs and some OC type IA chondrules; both could be made by oxygen isotope exchange between CAI melt and ambient ^{16}O-poor gas.

(4) The OC ARCs of this study experienced mild low-T metasomatism, including bleaching of chondrule mesostasis, replacing plagioclase with scapolite, and exchanging the mesostasis to be more ^{16}O-poor. In comparison with Na-Al-rich chondrules in metamorphosed OCs, we argue that these OC ARCs formed by metamorphism of Ca-Al-rich chondrules via bleaching, albitization, and dehydration during prograde thermal metamorphism.

Acknowledgments

The authors appreciate the assistance with SEM by Bil Schneider and with SIMS operation by Michael Spicuzza. We thank Maxime Piralla and two anonymous reviewers for their comprehensive and constructive comments that greatly improved the clarity and scientific significance of this paper. We gratefully acknowledge Yves Marrocchi for editorial handling. This work is supported by the NASA program (80NSSC21K0378, N.K.) and by the University of Wisconsin-Madison, Office of the Vice Chancellor for Research and Graduate Education, with funding from the Wisconsin Alumni Research Foundation. The WiscSIMS laboratory is supported by NSF (EAR-1658823, -2004618) and UW-Madison.

Appendix A. Supplementary material

The supplementary materials are: (1) BSE images of SIMS oxygen isotope analysis pit; BSE images and EDS results of SIMS Al-Mg isotope analysis pits; and optical images of LA-ICP-MS trace element analysis pits; (2) EPMA analysis condition, EPMA major element data, LA-ICP-MS trace element data, SIMS oxygen isotopes and Al-Mg isotopes data and related data processing; and (3) Four supplementary figures relating to the element distribution & correlation and bulk compositions of OC ARCs.

Data availability

Data are available through Mendeley Data at https://doi.org/10.17632/p3bt2wbcmj.1

References

Agee C., Burkemper L., Muttik N. and Spilde M. (2013) New primitive ordinary chondrite: Northwest Africa 7731 (L3. 00). *Meteoritics & Planetary Science Supplement* **76**, 5130.

Alexander C. M. O. D., Barber D. J. and Hutchison R. (1989) The microstructure of Semarkona and Bishunpur. *Geochim. Cosmochim. Acta* **53**, 3045-3057.

Alexander C. M. O. D., Grossman J. N., Ebel D. S. and Ciesla F. J. (2008) The Formation Conditions of Chondrules and Chondrites. *Science* **320**, 1617-1619.

Alexander C. M. O. D., Bowden R., Fogel M. L. and Howard K. T. (2015) Carbonate abundances and isotopic compositions in chondrites. *Meteorit. Planet. Sci* **50**, 810-833.

Barosch J., Hezel D. C., Ebel D. S. and Friend P. (2019) Mineralogically zoned chondrules in ordinary chondrites as evidence for open system chondrule behaviour. *Geochim. Cosmochim. Acta* **249**, 1-16.

Bischoff A. and Keil K. (1983) Ca-Al-rich chondrules and inclusions in ordinary chondrites. *Nature* **303**, 588-592.

Bischoff A. and Keil K. (1984) Al-rich objects in ordinary chondrites: Related origin of carbonaceous and ordinary chondrites and their constituents. *Geochim. Cosmochim. Acta* **48**, 693-709.

Bischoff A., Palme H. and Spettel B. (1989) Al-rich chondrules from the Ybbsitz H4-chondrite: evidence for formation by collision and splashing. *Earth Planet. Sci Lett.* **93**, 170-180.

Bollard J., Kawasaki N., Sakamoto N., Olsen M., Itoh S., Larsen K., Wielandt D., Schiller M., Connelly J. N., Yurimoto H. and Bizzarro M. (2019) Combined U-corrected Pb-Pb dating and ^{26}Al-^{26}Mg systematics of individual chondrules – evidence for a reduced initial abundance of ^{26}Al amongst inner Solar System chondrules. *Geochim. Cosmochim. Acta* **260**, 62-83.

Bouden N., Villeneuve J., Marrocchi Y., Deloule E., Füri E., Gurenko A., Piani L., Thomassot E., Peres P. and Fernandes F. (2021) Triple Oxygen Isotope Measurements by Multi-Collector Secondary Ion Mass Spectrometry. *Frontiers in Earth Science* **8**: 601169.

Boynton W. V. (1975) Fractionation in the solar nebula: condensation of yttrium and the rare earth elements. *Geochim. Cosmochim. Acta* **39**, 569-584.

Bridges J. C., Alexander C. M. O. D., Hutchison R., Franchi I. A. and Pillinger C. T. (1997) Sodium-, chlorine-rich mesostases in Chainpur (LL3) and Parnallee (LL3) chondrules. *Meteorit. Planet. Sci* **32**, 555-565.

Catanzaro E. J., Murphy T. J., Garner E. L. and Shields W. R. (1966) Absolute isotopic abundance ratios and atomic weight of magnesium. *J. Res. NBS* **70**, 453-458.

Clayton R. N., Grossman L. and Mayeda T. K. (1973) A component of primitive nuclear composition in carbonaceous meteorites. *Science* **182**, 485-488.

Cuzzi J. N. and Alexander C. M. D. (2006) Chondrule formation in particle-rich nebular regions at least hundreds of kilometres across. *Nature* **441**, 483-485.

Davis A. M. and Grossman L. (1979) Condensation and fractionation of rare earths in the solar nebula. *Geochim. Cosmochim. Acta* **43**, 1611-1632.

Davis A. M., Richter F. M., Mendybaev R. A., Janney P. E., Wadhwa M. and McKeegan K. D. (2015) Isotopic mass fractionation laws for magnesium and their effects on ^{26}Al–^{26}Mg systematics in solar system materials. *Geochim. Cosmochim. Acta* **158**, 245-261.

Davis A. M., Zhang J., Greber N. D., Hu J., Tissot F. L. H. and Dauphas N. (2018) Titanium isotopes and rare earth patterns in CAIs: Evidence for thermal processing and gas-dust decoupling in the protoplanetary disk. *Geochim. Cosmochim. Acta* **221**, 275-295.

Desch S. J., Kalyaan A. and Alexander C. M. O. D. (2018) The effect of Jupiter's formation on the distribution of refractory elements and inclusions in meteorites. *Astrophys. J. Suppl. Ser.* **238**, 11.

933 Dobrică E. and Brearley A. J. (2014) Widespread hydrothermal alteration minerals in the fine-grained matrices of
934 the Tieschitz unequilibrated ordinary chondrite. *Meteorit. Planet. Sci* **49**, 1323-1349.

935 Dobrică E., Le Guillou C. and Brearley A. J. (2019) Aqueous Alteration of Porous Microchondrules in Semarkona:
936 Implications for Hydration, Oxidation and Elemental Exchange Processes. *Geochim. Cosmochim. Acta* **244**,
937 292-307.

938 Dobrică E. and Brearley A. J. (2021) Iron-rich olivine in the unequilibrated ordinary chondrite, MET 00526: Earliest
939 stages of formation. *Meteorit. Planet. Sci* **55**, 2652-2669.

940 Ebel D. S. and Grossman L. (2000) Condensation in dust-enriched systems. *Geochim. Cosmochim. Acta* **64**, 339-366.

941 Ebert S. and Bischoff A. (2016) Genetic relationship between Na-rich chondrules and Ca,Al-rich inclusions? –
942 Formation of Na-rich chondrules by melting of refractory and volatile precursors in the solar nebula. *Geochim.*
943 *Cosmochim. Acta* **177**, 182-204.

944 Ebert S., Render J., Brennecka G. A., Burkhardt C., Bischoff A., Gerber S. and Kleine T. (2018) Ti isotopic
945 evidence for a non-CAI refractory component in the inner Solar System. *Earth Planet. Sci Lett.* **498**, 257-265.

946 Ebert S., Nagashima K., Bischoff A., Berndt J. and Krot A. N. (2022) Mineralogy, petrology, and oxygen isotopic
947 compositions of aluminum-rich chondrules from unequilibrated ordinary and the Dar al Gani 083 (CO3.1)
948 chondrite. *Geochim. Cosmochim. Acta* **336**, 448-468.

949 Faure F., Trolliard G., Nicollet C. and Montel J.-M. (2003) A developmental model of olivine morphology as a
950 function of the cooling rate and the degree of undercooling. *Contrib. Miner. Petrol.* **145**, 251-263.

951 Faure F. and Tissandier L. (2014) Contrasted Liquid Lines of Descent Revealed by Olivine-hosted Melt Inclusions
952 and the External Magma. *J. Petrol.* **55**, 1779-1798.

953 Faure F., Auxerre M. and Casola V. (2022) Slow cooling during crystallisation of barred olivine chondrules. *Earth*
954 *Planet. Sci Lett.* **593**, 117649.

955 Friend P., Hezel D. C. and Mucerschi D. (2016) The conditions of chondrule formation, Part II: Open system.
956 *Geochim. Cosmochim. Acta* **173**, 198-209.

957 Fukuda K., Beard B. L., Dunlap D. R., Spicuzza M. J., Fournelle J. H., Wadhwa M. and Kita N. T. (2020)
958 Magnesium isotope analysis of olivine and pyroxene by SIMS: Evaluation of matrix effects. *Chem. Geol* **540**,
959 119482.

960 Fukuda K., Tenner T. J., Kimura M., Tomioka N., Siron G., Ushikubo T., Chaumard N., Hertwig A. T. and Kita N.
961 T. (2022) A temporal shift of chondrule generation from the inner to outer Solar System inferred from oxygen
962 isotopes and Al-Mg chronology of chondrules from primitive CM and CO chondrites. *Geochim. Cosmochim.*
963 *Acta* **322**, 194-226.

964 Galy A., Young E. D., Ash R. D. and Keith O'Nions R. (2000) The Formation of Chondrules at High Gas Pressures
965 in the Solar Nebula. *Science* **290**, 1751-1753.

966 Gooding J. L., Keil K., Fukuoka T. and Schmitt R. A. (1980) Elemental abundances in chondrules from
967 unequilibrated chondrites: Evidence for chondrule origin by melting of pre-existing materials. *Earth Planet.*
968 *Sci Lett.* **50**, 171-180.

969 Goodrich C. A., Zolensky M. E., Fioretti A. M., Shaddad M. H., Downes H., Hiroi T., Kohl I., Young E. D., Kita N.
970 T., Hamilton V. E., Riebe M. E. I., Busemann H., Macke R. J., Fries M., Ross D. K. and Jenniskens P. (2019)
971 The first samples from Almahata Sitta showing contacts between ureilitic and chondritic lithologies:
972 Implications for the structure and composition of asteroid 2008 TC3. *Meteorit. Planet. Sci* **54**, 2769-2813.

973 Grossman J. N. and Wasson J. T. (1982) Evidence for primitive nebular components in chondrules from the
974 Chainpur chondrite. *Geochim. Cosmochim. Acta* **46**, 1081-1099.

975 Grossman J. N. and Wasson J. T. (1983) Refractory precursor components of Semarkona chondrules and the
976 fractionation of refractory elements among chondrites. *Geochim. Cosmochim. Acta* **47**, 759-771.

977 Grossman J. N., Alexander C. M. O. D., Wang J. and Brearley A. J. (2000) Bleached chondrules: Evidence for
978 widespread aqueous processes on the parent asteroids of ordinary chondrites. *Meteorit. Planet. Sci* **35**, 467-
979 486.

980 Grossman J. N., Alexanders C. M. O. D., Wang J. and Brearley A. J. (2002) Zoned chondrules in Semarkona:
981 Evidence for high- and low-temperature processing. *Meteorit. Planet. Sci* **37**, 49-73.

982 Grossman J. N. and Brearley A. J. (2005) The onset of metamorphism in ordinary and carbonaceous chondrites.
983 *Meteorit. Planet. Sci* **40**, 87-122.

984 Grossman L. (1973) Refractory trace elements in Ca-Al-rich inclusions in the Allende meteorite. *Geochim.*
985 *Cosmochim. Acta* **37**, 1119-1140.

986 Grossman L. and Ganapathy R. (1975) Volatile elements in Allende inclusions, Lunar Planet. Sci., Houston, pp.
987 1729-1736.

988 Grossman L. and Ganapathy R. (1976a) Trace elements in the Allende meteorite—II. Fine-grained. Ca-rich
989 inclusions. *Geochim. Cosmochim. Acta* **40**, 967-977.

990 Grossman L. and Ganapathy R. (1976b) Trace elements in the Allende meteorite—I. Coarse-grained, Ca-rich
991 inclusions. *Geochim. Cosmochim. Acta* **40**, 331-344.

992 Haugbølle T., Weber P., Wielandt D. P., Benítez-Llambay P., Bizzarro M., Gressel O. and Pessah M. E. (2019)
993 Probing the Protosolar Disk Using Dust Filtering at Gaps in the Early Solar System. *Astrophys. J.* **158**, 55.

994 Heck P. R., Ushikubo T., Schmitz B., Kita N. T., Spicuzza M. J. and Valley J. W. (2010) A single asteroidal source
995 for extraterrestrial Ordovician chromite grains from Sweden and China: High-precision oxygen three-isotope
996 SIMS analysis. *Geochim. Cosmochim. Acta* **74**, 497-509.

997 Hertwig A. T., Defouilloy C. and Kita N. T. (2018) Formation of chondrules in a moderately high dust enriched disk:
998 evidence from oxygen isotopes of chondrules from the Kaba CV3 chondrite. *Geochim. Cosmochim. Acta* **224**,
999 116-131.

1000 Hertwig A. T., Makoto K., Ushikubo T., Defouilloy C. and Kita N. T. (2019) The ^{26}Al-^{26}Mg systematics of FeO-
1001 rich chondrules from Acfer 094: two chondrule generations distinct in age and oxygen isotope ratios.
1002 *Geochim. Cosmochim. Acta* **253**, 111-126.

1003 Hewins R. H. and Radomsky P. M. (1990) Temperature conditions for chondrule formation. *Meteoritics* **25**, 309-318.

1004 Houlier B., Jaoul O., Abel F. and Liebermann R. C. (1988) Oxygen and silicon self-diffusion in natural olivine at T
1005 = 1300°C. *Phys. Earth Planet. Inter.* **50**, 240-250.

1006 Huang S., Farkaš J., Yu G., Petaev M. I. and Jacobsen S. B. (2012) Calcium isotopic ratios and rare earth element
1007 abundances in refractory inclusions from the Allende CV3 chondrite. *Geochim. Cosmochim. Acta* **77**, 252-265.

1008 Huss G. R., MacPherson G. J., Wasserburg G. J., Russell S. S. and Srinivasan G. (2001) Aluminum-26 in calcium-
1009 aluminum-rich inclusions and chondrules from unequilibrated ordinary chondrites. *Meteorit. Planet. Sci* **36**,
1010 975-997.

1011 Huss G. R., Rubin A. E. and Grossman J. N. (2006) Thermal metamorphism in chondrites.In *Meteorites and the*
1012 *Early Solar System II* (eds. D. Lauretta, L. A. Leshin, and Jr. H. Y. McSween). University of Arizona Press,
1013 Tucson, pp.567–586.

1014 Hutcheon I. D. and Hutchison R. (1989) Evidence from the Semarkona ordinary chondrite for ^{26}Al heating of small
1015 planets. *Nature* **337**, 238-241.

1016 Hutchison R., Alexander C. M. O. and barber D. J. (1987) The Semarkona meteorite: First recorded occurrence of
1017 smectite in an ordinary chondrite, and its implications. *Geochim. Cosmochim. Acta* **51**, 1875-1882.

1018 Jacobsen B., Yin Q.-Z., Moynier F., Amelin Y., Krot A. N., Nagashima K., Hutcheon I. D. and Palme H. (2008)
1019 ^{26}Al-^{26}Mg and ^{207}Pb-^{206}Pb systematics of Allende CAIs: Canonical solar initial ^{26}Al/^{27}Al ratio reinstated.
1020 *Earth Planet. Sci Lett.* **272**, 353-364.

1021 Jacquet E., Fromang S. and Gounelle M. (2011) Radial transport of refractory inclusions and their preservation in
1022 the dead zone. *Astron. Astrophys* **526**, L8.

Jiang Y., Hsu W., Guan Y. and Wang Y. (2015) In situ SIMS oxygen isotope analyses: Evidence for the formation of aluminum-rich chondrules from ordinary chondrites. *Science China Earth Sciences* **58**, 1748-1757.

Jochum K. P., Willbold M., Raczek I., Stoll B. and Herwig K. (2005) Chemical Characterisation of the USGS Reference Glasses GSA-1G, GSC-1G, GSD-1G, GSE-1G, BCR-2G, BHVO-2G and BIR-1G Using EPMA, ID-TIMS, ID-ICP-MS and LA-ICP-MS. *Geostandards and Geoanalytical Research* **29**, 285-302.

Jochum K. P., Stoll B., Herwig K., Willbold M., Hofmann A. W., Amini M., Aarburg S., Abouchami W., Hellebrand E. and Mocek B. (2006) MPI-DING reference glasses for in situ microanalysis: New reference values for element concentrations and isotope ratios. *Geochemistry, Geophysics, Geosystems* **7**, Q02008.

Jones R. H. and Scott E. R. D. (1989) Petrology and thermal history of type IA chondrules in the Semarkona (LL3. 0) chondrite, Lunar Planet. Sci., Houston, pp. 523-536.

Jones R. H. (1994) Petrology of FeO-poor, porphyritic pyroxene chondrules in the Semarkona chondrite. *Geochim. Cosmochim. Acta* **58**, 5325-5340.

Jones R. H. and Layne G. D. (1997) Minor and trace element partitioning between pyroxene and melt in rapidly cooled chondrules. *Am. Mineral* **82**, 534-545.

Jones R. H., McCubbin F. M., Dreeland L., Guan Y., Burger P. V. and Shearer C. K. (2014) Phosphate minerals in LL chondrites: A record of the action of fluids during metamorphism on ordinary chondrite parent bodies. *Geochim. Cosmochim. Acta* **132**, 120-140.

Kadlag Y., Tatzel M., Frick D. A. and Becker H. (2019) The origin of unequilibrated EH chondrites – Constraints from in situ analysis of Si isotopes, major and trace elements in silicates and metal. *Geochim. Cosmochim. Acta* **267**, 300-321.

Kadlag Y., Tatzel M., Frick D. A., Becker H. and Kühne P. (2021) In situ Si isotope and chemical constraints on formation and processing of chondrules in the Allende meteorite. *Geochim. Cosmochim. Acta* **304**, 234-257.

Kennedy A., Lofgren G. and Wasserburg G. (1993) An experimental study of trace element partitioning between olivine, orthopyroxene and melt in chondrules: equilibrium values and kinetic effects. *Earth Planet. Sci Lett.* **115**, 177-195.

Kimura M., Grossman J. N. and Weisberg M. K. (2008) Fe-Ni metal in primitive chondrites: Indicators of classification and metamorphic conditions for ordinary and CO chondrites. *Meteorit. Planet. Sci* **43**, 1161-1177.

Kita N. T., Nagahara H., Togashi S. and Morishita Y. (2000) A short duration of chondrule formation in the solar nebula: evidence from ^{26}Al in Semarkona ferromagnesian chondrules. *Geochim. Cosmochim. Acta* **64**, 3913-3922.

Kita N. T., Nagahara H., Tachibana S., Tomomura S., Spicuzza M. J., Fournelle J. H. and Valley J. W. (2010) High precision SIMS oxygen three isotope study of chondrules in LL3 chondrites: Role of ambient gas during chondrule formation. *Geochim. Cosmochim. Acta* **74**, 6610-6635.

Kita N. T., Ushikubo T., Knight K. B., Mendybaev R. A., Davis A. M., Richter F. M. and Fournelle J. H. (2012) Internal ^{26}Al–^{26}Mg isotope systematics of a Type B CAI: Remelting of refractory precursor solids. *Geochim. Cosmochim. Acta* **86**, 37-51.

Krot A. N. and Rubin A. E. (1994) Glass-rich chondrules in ordinary chondrites. *Meteoritics* **29**, 697-707.

Krot A. N., Zolensky M. E., Wasson J. T., Scott E. R. D., Keil K. and Ohsumi K. (1997) Carbide-magnetite assemblages in type-3 ordinary chondrites. *Geochim. Cosmochim. Acta* **61**, 219-237.

Krot A. N., Fagan T. J., Keil K., McKeegan K. D., Sahijpal S., Hutcheon I. D., Petaev M. I. and Yurimoto H. (2004a) Ca,Al-rich inclusions, amoeboid olivine aggregates, and Al-rich chondrules from the unique carbonaceous chondrite Acfer 094: I. mineralogy and petrology. *Geochim. Cosmochim. Acta* **68**, 2167-2184.

Krot A. N., MacPherson G. J., Ulyanov A. A. and Petaev M. I. (2004b) Fine-grained, spinel-rich inclusions from the reduced CV chondrites Efremovka and Leoville: I. Mineralogy, petrology, and bulk chemistry. *Meteorit. Planet. Sci* **39**, 1517-1553.

Kurat G., Pernicka E. and Herrwerth I. (1984) Chondrules from Chainpur (LL-3): reduced parent rocks and vapor fractionation. *Earth Planet. Sci Lett.* **68**, 43-56.

Larsen K. K., Trinquier A., Paton C., Schiller M., Wielandt D., Ivanova M. A., Connelly J. N., Nordlund Å., Krot A. N. and Bizzarro M. (2011) Evidence for magnesium isotope heterogeneity in the solar protoplanetary disk. *Astrophys. J. Lett.* **735**, L37.

LaTourrette, T. and Wasserburg G. J. (1998) Mg diffusion in anorthite: implications for the formation of early solar system planetesimals. *Earth Planet. Sci Lett.* **158**, 91-108.

Lesher C. E., Hervig R. L. and Tinker D. (1996) Self diffusion of network formers (silicon and oxygen) in naturally occurring basaltic liquid. *Geochim. Cosmochim. Acta* **60**, 405-413.

Lewis J. A. and Jones R. H. (2019) Primary feldspar in the Semarkona LL3.00 chondrite: Constraints on chondrule formation and secondary alteration. *Meteorit. Planet. Sci* **54**, 72-89.

Lewis J. A., Jones R. H. and Brearley A. J. (2022) Plagioclase alteration and equilibration in ordinary chondrites: Metasomatism during thermal metamorphism. *Geochim. Cosmochim. Acta* **316**, 201-229.

Libourel G. (1999) Systematics of calcium partitioning between olivine and silicate melt: implications for melt structure and calcium content of magmatic olivines. *Contrib. Miner. Petrol.* **136**, 63-80.

Libourel G., Krot A. and Tissandier L. (2006) Role of gas-melt interaction during chondrule formation. *Earth Planet. Sci Lett.* **251**, 232-240.

Libourel G. and Portail M. (2018) Chondrules as direct thermochemical sensors of solar protoplanetary disk gas. *Science Advances* **4**, eaar3321.

Lin Y. and Kimura M. (1998) Anorthite-spinel-rich inclusions in the Ningqiang carbonaceous chondrite: Genetic links with Type A and C inclusions. *Meteorit. Planet. Sci* **33**, 435-446.

Lodders K. (2003) Solar System Abundances and Condensation Temperatures of the Elements. *Astrophys. J.* **591**, 1220-1247.

Lofgren G. and Lanier A. B. (1990) Dynamic crystallization study of barred olivine chondrules. *Geochim. Cosmochim. Acta* **54**, 3537-3551.

Ludwig K. R. (2012) User's manual for Isoplot 3.75: A geochronological toolkit for Microsoft Excel, Berkeley Geochronology Centre, Berkeley (Spe. Pub. 5).

MacPherson G. J. and Huss G. R. (2005) Petrogenesis of Al-rich chondrules: Evidence from bulk compositions and phase equilibria. *Geochim. Cosmochim. Acta* **69**, 3099-3127.

Marrocchi Y., Villeneuve J., Batanova V., Piani L. and Jacquet E. (2018) Oxygen isotopic diversity of chondrule precursors and the nebular origin of chondrules. *Earth Planet. Sci Lett.* **496**, 132-141.

Marrocchi Y., Euverte R., Villeneuve J., Batanova V., Welsch B., Ferrière L. and Jacquet E. (2019) Formation of CV chondrules by recycling of amoeboid olivine aggregate-like precursors. *Geochim. Cosmochim. Acta* **247**, 121-141.

Marrocchi Y., Longeau A., Goupil R. L., Dijon V., Pinto G., Neukampf J., Villeneuve J. and Jacquet E. (2024) Isotopic evolution of the inner solar system revealed by size-dependent oxygen isotopic variations in chondrules. *Geochim. Cosmochim. Acta* **371**, 52-64.

Martin P. M. and Mason B. (1974) Major and trace elements in the Allende meteorite. *Nature* **249**, 333-334.

Martins R., Chaussidon M., Deng Z., Pignatale F. and Moynier F. (2021) A condensation origin for the mass-dependent silicon isotopic variations in Allende components: implications for complementarity. *Earth Planet. Sci Lett.* **554**, 116678.

Mason B. and Martin P. M. (1977) Geochemical differences among components of the Allende meteorite. *Smithsonian Contribution to the Earth Sciences* **19**, 84-95.

Mason B. and Taylor S. R. (1982) Inclusions in the Allende meteorite. *Smithsonian Contribution to the Earth Sciences* **25**, 1-30.

Mishra R. K., Goswami J. N., Tachibana S., Huss G. R. and Rudraswami N. G. (2010) ^{60}Fe and ^{26}Al in Chondrules from Unequilibrated Chondrites: Implications for Early Solar System Processes. *Astrophys. J. Lett.* **714**, L217.

Nagahara H., Kita N. T., Ozawa K. and Morishita Y. (2008) Condensation of major elements during chondrule formation and its implication to the origin of chondrules. *Geochim. Cosmochim. Acta* **72**, 1442-1465.

Nagashima K., Krot A. N. and Komatsu M. (2017) ^{26}Al-^{26}Mg systematics in chondrules from Kaba and Yamato 980145 CV3 carbonaceous chondrites. *Geochim. Cosmochim. Acta* **201**, 303-319.

Nishiizumi K. (2004) Preparation of ^{26}Al AMS standards. *Nuclear Instruments and Methods in Physics Research Section B: Beam Interactions with Materials and Atoms* **223-224**, 388-392.

Pape J., Mezger K., Bouvier A. S. and Baumgartner L. P. (2019) Time and duration of chondrule formation: Constraints from ^{26}Al-^{26}Mg ages of individual chondrules. *Geochim. Cosmochim. Acta* **244**, 416-436.

Paton C., Hellstrom J., Paul B., Woodhead J. and Hergt J. (2011) Iolite: Freeware for the visualisation and processing of mass spectrometric data. *J. Anal. At. Spectrom.* **26**, 2508-2518.

Pearce N. J., Perkins W. T., Westgate J. A., Gorton M. P., Jackson S. E., Neal C. R. and Chenery S. P. (1997) A compilation of new and published major and trace element data for NIST SRM 610 and NIST SRM 612 glass reference materials. *Geostandards newsletter* **21**, 115-144.

Piralla M., Villeneuve J., Batanova V., Jacquet E. and Marrocchi Y. (2021) Conditions of chondrule formation in ordinary chondrites. *Geochim. Cosmochim. Acta* **313**, 295-312.

Piralla M., Villeneuve J., Schnuriger N., Bekaert D. V. and Marrocchi Y. (2023) A unified chronology of dust formation in the early solar system. *Icarus*, 115427.

Ross D., Simon J. and Cato M. (2017) Spinel-Bearing, Al-Rich Chrondrules in the Unequilibrated Ordinary Chondrite NWA7402, Lunar Planet. Sci., Houston, p. 1964.

Rubin A. E. and Grossman J. N. (1985) Phospate-sulfide assemblages and Al/Ca ratios in type-3 chondrites. *Meteoritics* **20**, 479-489.

Rubin A. E. and Pernicka E. (1989) Chondrules in the Sharps H3 chondrite: Evidence for intergroup compositional differences among ordinary chondrite chondrules. *Geochim. Cosmochim. Acta* **53**, 187-195.

Rubin A. E. (2004) Aluminian low-Ca pyroxene in a Ca-Al-rich chondrule from the Semarkona meteorite. *Am. Mineral* **89**, 867-872.

Rudraswami N. G. and Goswami J. N. (2007) ^{26}Al in chondrules from unequilibrated L chondrites: Onset and duration of chondrule formation in the early solar system. *Earth Planet. Sci Lett.* **257**, 231-244.

Rudraswami N. G., Goswami J. N., Chattopadhyay B., Sengupta S. K. and Thapliyal A. P. (2008) ^{26}Al records in chondrules from unequilibrated ordinary chondrites: II. Duration of chondrule formation and parent body thermal metamorphism. *Earth Planet. Sci Lett.* **274**, 93-102.

Russell S. S., Srinivasan G., Huss G. R., Wasserburg G. J. and MacPherson G. J. (1996) Evidence for widespread ^{26}Al in the solar nebula and constraints for nebula time scales. *Science* **273**, 757-762.

Russell S., Huss G., MacPherson G. and Wasserburg G. (1997) Early and late chondrule formation: New constraints for solar nebula chronology from 26Al/27Al in unequilibrated ordinary chondrites, Lunar Planet. Sci., Houston, p. 1209.

Russell S. S., MacPherson G. J., Leshin L. A. and McKeegan K. D. (2000) ^{16}O enrichments in aluminum-rich chondrules from ordinary chondrites. *Earth Planet. Sci Lett.* **184**, 57-74.

Russell S. S., Connolly Jr. H. C. and Krot A. N. (2018) Chondrules: Records of Protoplanetary Disk Processes. Cambridge University Press, Cambridge.

Ruzicka A., Grossman J., Bouvier A. and Agee C. B. (2017) The Meteoritical Bulletin, No. 103. *Meteorit. Planet. Sci* **52**, 1014.

Ryerson F. J. and McKeegan K. D. (1994) Determination of oxygen self-diffusion in åkermanite, anorthite, diopside, and spinel: Implications for oxygen isotopic anomalies and the thermal histories of Ca-Al-rich inclusions. *Geochim. Cosmochim. Acta* **58**, 3713-3734.

Shelby J. E. (1985) Formation and Properties of Calcium Aluminosilicate Glasses. *Journal of the American Ceramic Society* **68**, 155-158.

Sheng Y. J., Hutcheon I. D. and Wasserburg G. J. (1991) Origin of plagioclase-olivine inclusions in carbonaceous chondrites. *Geochim. Cosmochim. Acta* **55**, 581-599.

Siron G., Fukuda K., Kimura M. and Kita N. T. (2021) New constraints from ^{26}Al-^{26}Mg chronology of anorthite bearing chondrules in unequilibrated ordinary chondrites. *Geochim. Cosmochim. Acta* **293**, 103-126.

Siron G., Fukuda K., Kimura M. and Kita N. T. (2022) High precision ^{26}Al-^{26}Mg chronology of chondrules in unequilibrated ordinary chondrites: Evidence for restricted formation ages. *Geochim. Cosmochim. Acta* **324**, 312-345.

Swindle T. D., Grossman J. N., Olinger C. T. and Garrison D. H. (1991) Iodine-xenon, chemical, and petrographie studies of Semarkona chondrules: Evidence for the timing of aqueous alteration. *Geochim. Cosmochim. Acta* **55**, 3723-3734.

Sylvester P. J., Simon S. B. and Grossman L. (1993) Refractory inclusions from the Leoville, Efremovka, and Vigarano C3V chondrites: Major element differences between types A and B, and extraordinary refractory siderophile element compositions. *Geochim. Cosmochim. Acta* **57**, 3763-3784.

Tachibana S., Nagahara H., Mostefaoui S. and Kita N. (2003) Correlation between relative ages inferred from ^{26}Al and bulk compositions of ferromagnesian chondrules in least equilibrated ordinary chondrites. *Meteorit. Planet. Sci* **38**, 939-962.

Tachibana S. and Huss G. R. (2005) Sulfur isotope composition of putative primary troilite in chondrules from Bishunpur and Semarkona. *Geochim. Cosmochim. Acta* **69**, 3075-3097.

Tenner T. J., Nakashima D., Ushikubo T., Kita N. T. and Weisberg M. K. (2015) Oxygen isotope ratios of FeO-poor chondrules in CR3 chondrites: Influence of dust enrichment and H_2O during chondrule formation. *Geochim. Cosmochim. Acta* **148**, 228-250.

Tenner T. J., Nakashima D., Ushikubo T., Tomioka N., Kimura M., Weisberg M. K. and Kita N. T. (2019) Extended chondrule formation intervals in distinct physicochemical environments: Evidence from Al-Mg isotope systematics of CR chondrite chondrules with unaltered plagioclase. *Geochim. Cosmochim. Acta* **260**, 133-160.

Tissandier L., Libourel G. and Robert F. (2002) Gas-melt interactions and their bearing on chondrule formation. *Meteorit. Planet. Sci* **37**, 1377-1389.

Torrano Z. A., Brennecka G. A., Williams C. D., Romaniello S. J., Rai V. K., Hines R. R. and Wadhwa M. (2019) Titanium isotope signatures of calcium-aluminum-rich inclusions from CV and CK chondrites: Implications for early Solar System reservoirs and mixing. *Geochim. Cosmochim. Acta* **263**, 13-30.

Torrano Z. A., Brennecka G. A., Mercer C. M., Romaniello S. J., Rai V. K., Hines R. R. and Wadhwa M. (2023) Titanium and chromium isotopic compositions of calcium-aluminum-rich inclusions: Implications for the sources of isotopic anomalies and the formation of distinct isotopic reservoirs in the early Solar System. *Geochim. Cosmochim. Acta* **348**, 309-322.

Tronche E. J., Hewins R. H. and MacPherson G. J. (2007) Formation conditions of aluminum-rich chondrules. *Geochim. Cosmochim. Acta* **71**, 3361-3381.

Tsuchiyama A., Osada Y., Nakano T. and Uesugi K. (2004) Experimental reproduction of classic barred olivine chondrules: Open-system behavior of chondrule formation. *Geochim. Cosmochim. Acta* **68**, 653-672.

Ushikubo T., Kimura M., Kita N. T. and Valley J. W. (2012) Primordial oxygen isotope reservoirs of the solar nebula recorded in chondrules in Acfer 094 carbonaceous chondrite. *Geochim. Cosmochim. Acta* **90**, 242-264.

Ushikubo T., Nakashima D., Kimura M., Tenner T. J. and Kita N. T. (2013) Contemporaneous formation of chondrules in distinct oxygen isotope reservoirs. *Geochim. Cosmochim. Acta* **109**, 280-295.

Ushikubo T., Tenner T. J., Hiyagon H. and Kita N. T. (2017) A long duration of the ^{16}O-rich reservoir in the solar nebula, as recorded in fine-grained refractory inclusions from the least metamorphosed carbonaceous chondrites. *Geochim. Cosmochim. Acta* **201**, 103-122.

Van Orman J. A., Cherniak D. J., and Kita N. T. (2014) Magnesium diffusion in plagioclase: Dependence on composition, and implications for thermal resetting of the ^{26}Al–^{26}Mg early solar system chronometer. *Earth Planet. Sci Lett.* **385**, 79-88.

Varela M. E. and Zinner E. (2018) Unraveling the role of liquids during chondrule formation processes. *Geochim. Cosmochim. Acta* **221**, 358-378.

Villeneuve J., Chaussidon M. and Libourel G. (2009) Homogeneous distribution of ^{26}Al in the solar system from the Mg isotopic composition of chondrules. *Science* **325**, 985-988.

Villeneuve J., Marrocchi Y. and Jacquet E. (2020) Silicon isotopic compositions of chondrule silicates in carbonaceous chondrites and the formation of primordial solids in the accretion disk. *Earth Planet. Sci Lett.* **542**, 116318.

Wakaki S., Itoh S., Tanaka T. and Yurimoto H. (2013) Petrology, trace element abundances and oxygen isotopic compositions of a compound CAI–chondrule object from Allende. *Geochim. Cosmochim. Acta* **102**, 261-279.

Wänke H., Baddenhausen H., Palme H. and Spettel B. (1974) On the chemistry of the Allende inclusions and their origin as high temperature condensates. *Earth Planet. Sci Lett.* **23**, 1-7.

Wark D. A. (1987) Plagioclase-rich inclusions in carbonaceous chondrite meteorites: Liquid condensates? *Geochim. Cosmochim. Acta* **51**, 221-242.

Wick M. J. and Jones R. H. (2012) Formation conditions of plagioclase-bearing type I chondrules in CO chondrites: A study of natural samples and experimental analogs. *Geochim. Cosmochim. Acta* **98**, 140-159.

Young E. D. and Russell S. S. (1998) Oxygen reservoirs in the early solar nebula inferred from an Allende CAI. *Science* **282**, 452-455.

Zhang A.-C., Itoh S., Sakamoto N., Wang R.-C. and Yurimoto H. (2014) Origins of Al-rich chondrules: Clues from a compound Al-rich chondrule in the Dar al Gani 978 carbonaceous chondrite. *Geochim. Cosmochim. Acta* **130**, 78-92.

Zhang M., Bonato E., King A. J., Russell S. S., Tang G. and Lin Y. (2020a) Petrology and oxygen isotopic compositions of calcium-aluminum-rich inclusions in primitive CO3.0-3.1 chondrites. *Meteorit. Planet. Sci* **55**, 911-935.

Zhang M., Lin Y., Tang G., Liu Y. and Leya I. (2020b) Origin of Al-rich chondrules in CV chondrites: Incorporation of diverse refractory components into the ferromagnesian chondrule-forming region. *Geochim. Cosmochim. Acta* **272**, 198-217.

Zhang M., Fukuda K., Spicuzza M. J., Siron G., Heimann A., Hammerstrom A. J., Kita N. T., Ushikubo T. and Valley J. W. (2022) SIMS matrix effects in oxygen isotope analysis of olivine and pyroxene: Application to Acfer 094 chondrite chondrules and reconsideration of the primitive chondrule minerals (PCM) line. *Chem. Geol* **608**, 121016.

Zhang Y., Ni H. and Chen Y. (2010) Diffusion data in silicate melts. In: *Diffusion in Minerals and Melts* (eds. Y. Zhang and D. J. Cherniak). The Mineralogical Society of America, Chantilly, Virginia, pp. 311-408.

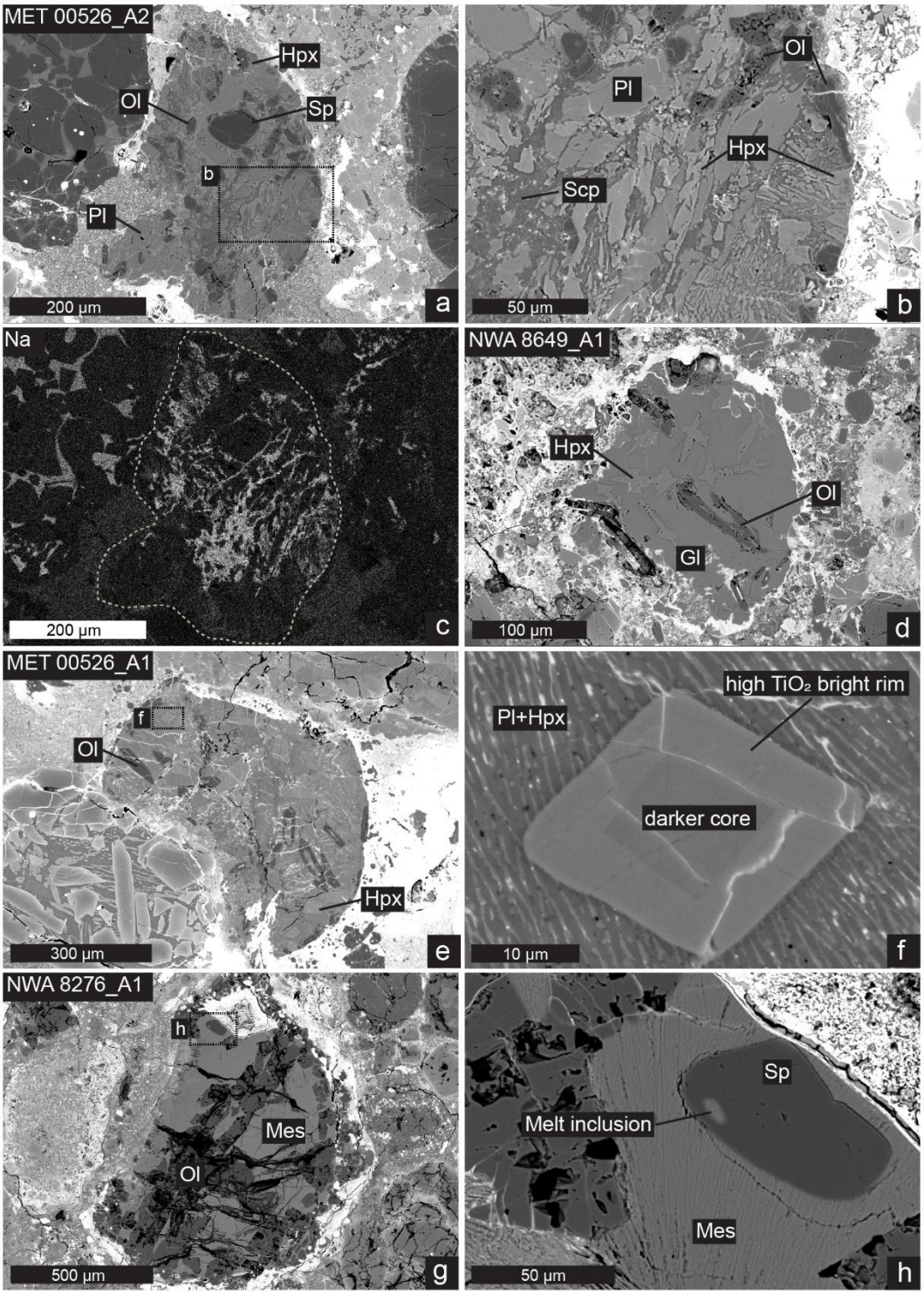

1242

1243 Fig. 1. Petrography of four OC ARCs in this study. (a, b) BSE images of MET 00526_A2 show it is a
1244 plagioclase-bearing chondrule composed of spinel, olivine, plagioclase, high-Ca pyroxene, and
1245 mesostasis of microcrystalline plagioclase and high-Ca pyroxene. Olivine occurs mainly as tablet

crystals and, occasionally, as anhedral crystals decorating the chondrule's surface. (c) X-ray elemental map of Na of MET 00526_A2 illustrates the distribution of scapolite within this chondrule. (d) NWA 8649_A1, an ovoid glassy ARC with an apparent diameter of ~200 μm. It has skeletal olivine and dendritic high-Ca pyroxene embedded in a clean Ca-Al-rich glass. (e, f) MET 00526_A1 (570 × 300 μm), a glassy ARC with curved sides, while its Y axis was squeezed by nearby large chondrules during accretion. It contains skeletal olivine and diamond-shaped or blocky high-Ca pyroxene, with the core being darker (lower TiO_2) than the rim. Its mesostasis is an intergrowth of microcrystalline plagioclase and high-Ca pyroxene immersed with many iron oxide veins formed by terrestrial weathering. (g, h) NWA 8276_A1, the largest ARC (1100 × 700 μm) of this study, is oval-shaped and composed mainly of olivine and mesostasis, with minor amounts of spinel and high-Ca pyroxene. It has a barred-olivine texture with parallel olivine bars located at the center of this chondrule. Blocky olivine crystals were observed to be aligned along the chondrule surface. Its mesostasis was slightly devitrified as feathery crystals likely plagioclase and high-Ca pyroxene. Abbreviations: Sp = spinel; Ol = olivine; Hpx= high-Ca pyroxene; Pl = plagioclase; Scp = Scapolite; Gl = glass; Mes = mesostasis.

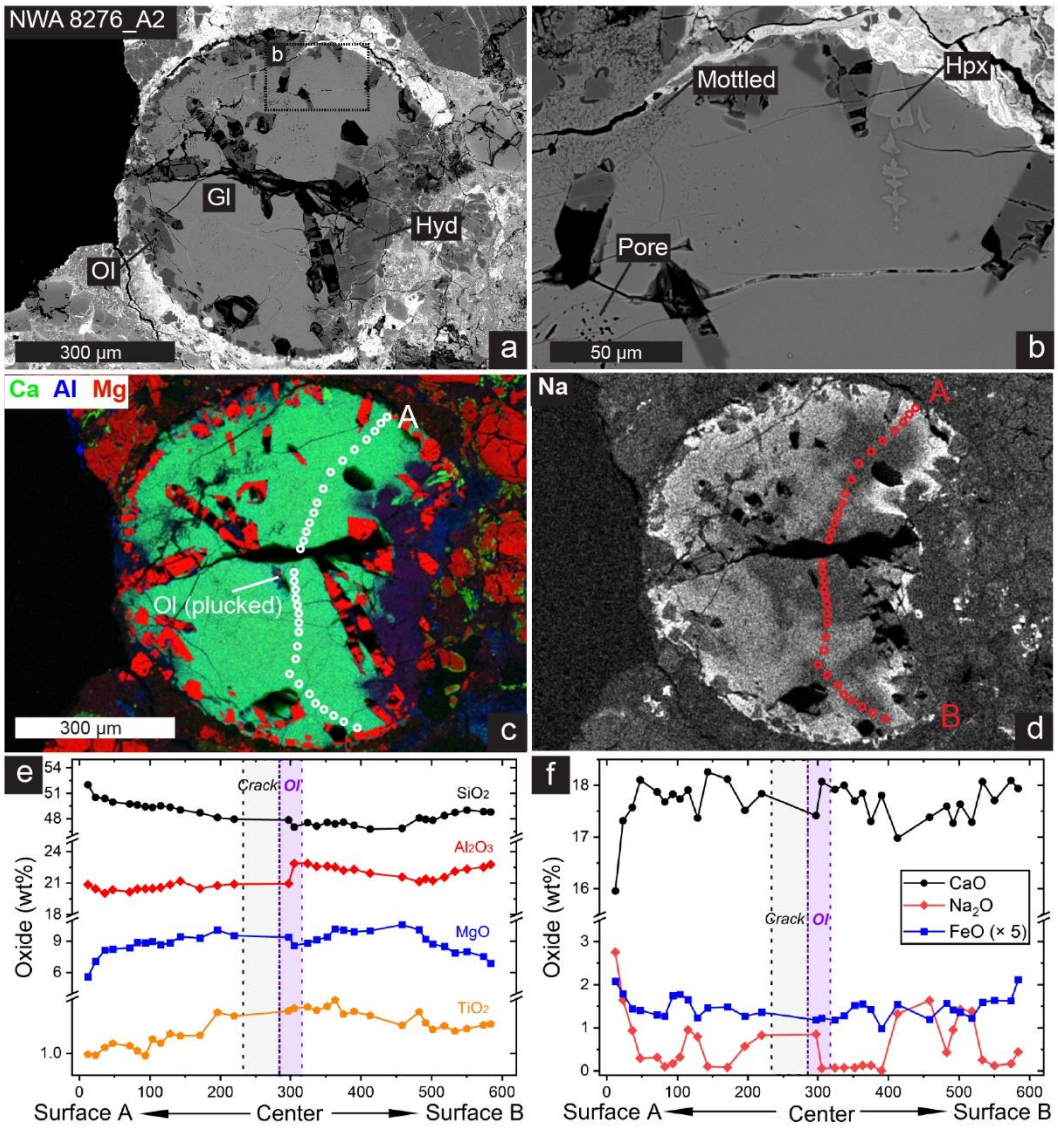

Fig. 2. Petrography and elemental distribution of the glassy ARC NWA 8276_A2. (a) BSE image shows a nearly round chondrule with an apparent diameter of ~580 μm, dominated by olivine and glassy mesostasis. Olivine is tablet and preferentially located at the margin of the chondrule with a long axis parallel or normal to the surface. Some interior olivine crystals were partially or completely plucked during sample preparation and left prismatic-shaped cavities. (b) An enlarged view shows a dendritic high-Ca pyroxene at the surface. Micron-sized pores and mottled regions ("Mottled") were randomly distributed in the mesostasis. (c) A combined X-ray elemental map (Ca: green, Al: blue, Mg: red) shows a hydrated phase (analysis total ~70 wt%) at the right side of this chondrule, likely formed by leaching the glassy mesostasis. (d) An X-ray elemental map of Na shows Na-rich

1275 domains are bracketed by Na-poor domains, and the interface between the hydrated phase and
1276 inferior glass mesostasis is significantly Na-rich. (e) Transverse EPMA analysis (A-B) shows
1277 chondrule-scale concentric zonation of MgO, SiO_2, and TiO_2 in the glassy mesostasis and symmetric
1278 zonation of Al_2O_3 in the lower half of this chondrule. It is noted that the abrupt increase of Al_2O_3 and
1279 TiO_2 and decrease of MgO and SiO_2 observed at the center resulted from a nearby olivine
1280 crystallization (indicated “plucked” in panel c). (f) EPMA line profiles of Na_2O, CaO, and FeO. The
1281 CaO profile is irregular and complementary to the Na_2O profile. The FeO profile is concentrically
1282 zoned like SiO_2. To plot the FeO profile in the same figure, it was shown as five times its actual
1283 contents (< 0.5 wt%). Abbreviations: Hyd = hydrated phase; Mottled = mottled region in glassy
1284 mesostasis; others are the same as in Fig. 1.
1285
1286
1287
1288

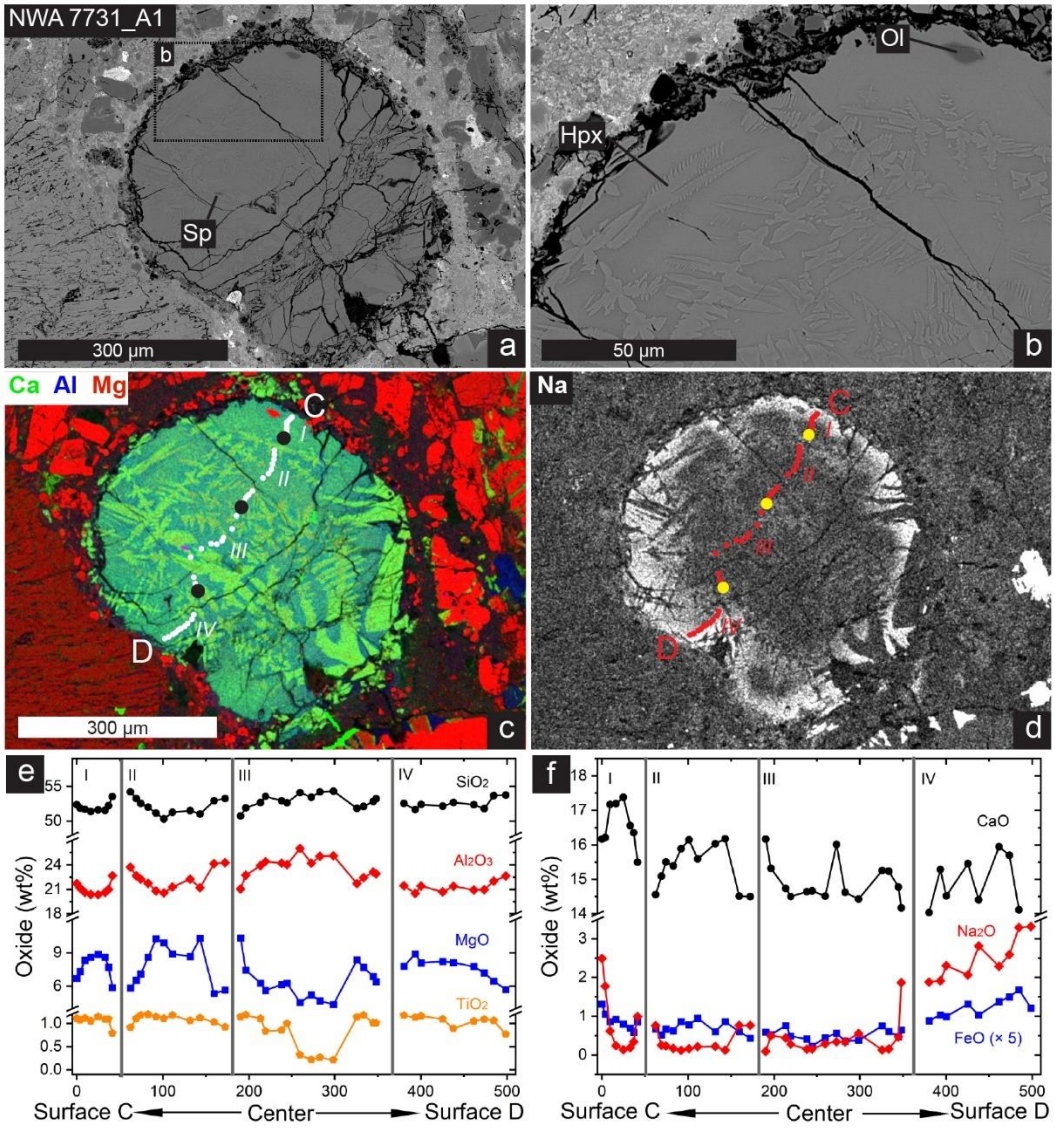

Fig. 3. Petrography and elemental distribution of the glassy ARC NWA 7731_A1. (a) BSE image shows it is round with an apparent diameter of ~440 μm. The periphery of this chondrule is almost vacant with minor amounts of high-Ca pyroxene and olivine fragments, which could be remnants of dissolving glassy mesostasis by asteroidal fluids. A skeletal-shaped cavity at its lower right could be a relic of an olivine crystal. (b) An enlarged view shows dendritic high-Ca pyroxene and clean glassy mesostasis. A blocky olivine grain was found at its upper margin. (c) A combined X-ray elemental map of Ca (green), Al (blue), and Mg (red) shows the dendritic shape of high-Ca pyroxene and its distribution. A tiny spinel grain (purple) was identified at the center. (d) X-ray elemental map of Na shows concentric zonation of Na_2O, with the outer ~100 μm region being richer in Na_2O than the

interior ~300 μm. Several slightly brighter subregions were observed in the interior. (e) Profiles of SiO_2, Al_2O_3, MgO, and TiO_2 show localized chemical zonation in segments I, II, and IV, which were separated by high-Ca pyroxene bars, while segment II that across a coarse high-Ca pyroxene shows opposite zonation. (f) Profiles of CaO, Na_2O, and FeO. CaO shows irregular distributions, while Na_2O (with small spikes) and FeO show concentric zonation. Abbreviations are the same as in Fig. 1.

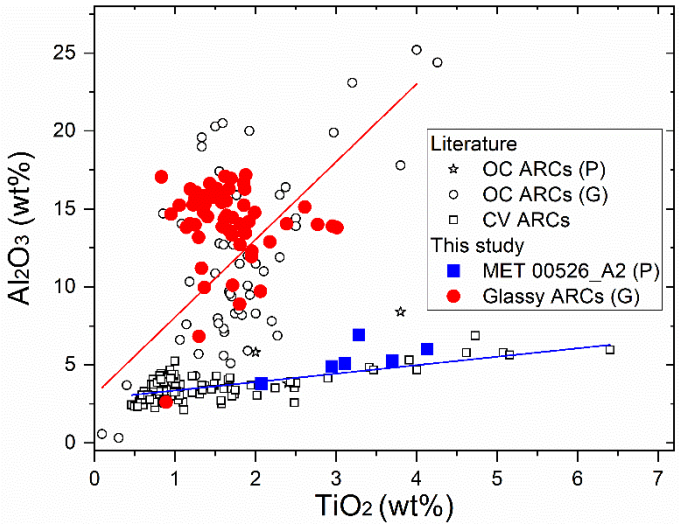

Fig. 4. Al_2O_3 vs. TiO_2 contents in high-Ca pyroxene of the six ARCs studied. High-Ca pyroxene from the plagioclase-bearing ARC ("P") MET 00526_A2 follows a linear trend with a slope of ~0.5 like other plagioclase-bearing OC ARCs (MacPherson and Huss, 2005) and porphyritic ARCs in CV chondrites (Zhang et al., 2020b). In contrast, high-Ca pyroxene from five glassy ARCs ("G") of this study has much higher Al_2O_3 that shows poor correlation with its TiO_2 contents, like other glassy OC ARCs in the literature (Krot and Rubin, 1994; MacPherson and Huss, 2005; Jiang et al., 2015; Ebert and Bischoff, 2016; Ebert et al., 2022).

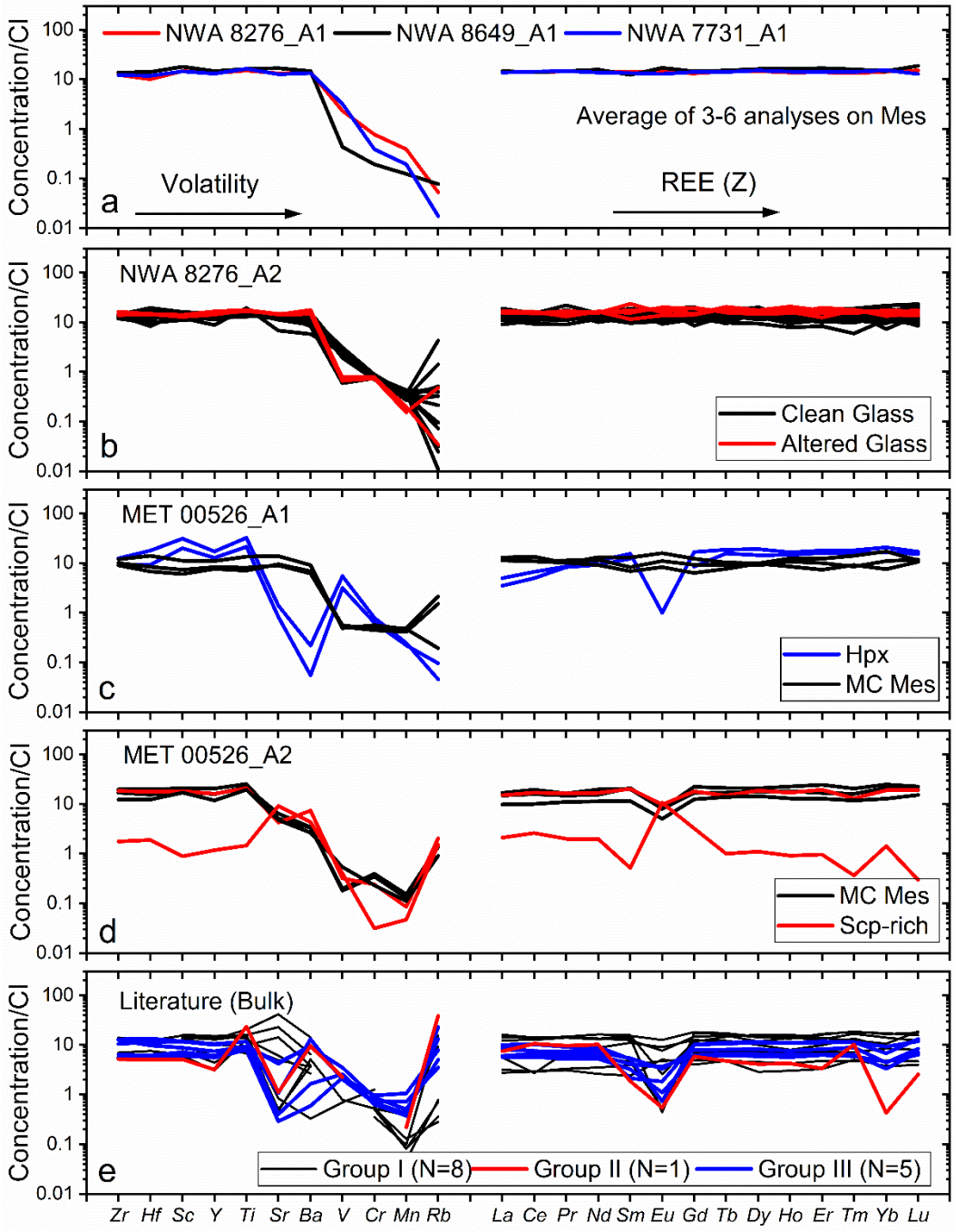

1314

1315 Fig. 5. Trace element abundances of mesostasis and/or high-Ca pyroxene in the six OC ARC
1316 studied. REEs are plotted separately from other trace elements. From left to right, other elements
1317 follow their order of volatility, and REEs follow their order of atomic number (Z). (a) Three to six
1318 analyses of NWA 8276_A1, NWA 8649_A1, and NWA 7731_A1 show uniform trace element
1319 concentrations and, for clarity, only average values are plotted. They show unfractionated RLE (Zr,

Hf, Sc, Y, Ti, Sr, Ba, and REE) patterns with varying depletions of V. The reason for V depletion is unknown. Abundances of Cr, Mn, Rb decrease as their volatility increases. (b) Individual analysis of NWA 8276_A2. Trace element abundances of mottled mesostasis are almost identical to the clean glass. (c) Individual analysis of high-Ca pyroxene and mesostasis in MET 00526_A1. High-Ca pyroxene shows enrichments of Sc, Ti, V, and HREEs compared to its microcrystalline mesostasis. (d) Individual analysis of MET 00526_A2. An analysis of scapolite shows complementary REEs to microcrystalline mesostasis. In contrast, another scapolite analysis is almost identical to mesostasis, which might have sampled a significant amount of mesostasis beneath. (d) Bulk trace elements of OC ARCs in literature, in which Groups I, II, and III are plotted in different colors (MacPherson and Huss, 2005; Ebert and Bischoff, 2016). Abbreviations: MC Mes = micro-crystalline mesostasis; others are the same as in Fig. 1.

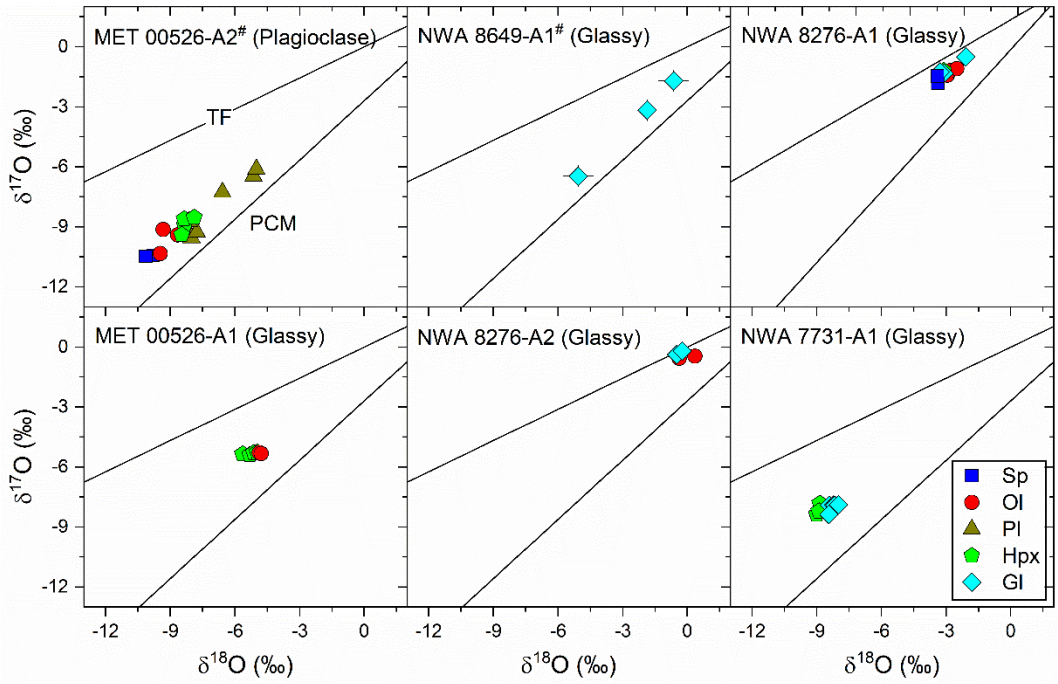

Fig. 6. Oxygen isotope ratios of major minerals in the six ARCs studied. MET 00526_A2 and NWA 8649_A1 display heterogeneity in the mass-independent fractionation of oxygen isotope (#), while the remaining four are homogeneous. Two analyses on the mottled regions of glassy mesostais in NWA 8276_A2, which show ~5 ‰ $\delta^{18}O$ and ~1 ‰ $\Delta^{17}O$, are not plotted. Abbreviations: TF = terrestrial fractionation line; PCM = primitive chondrule mineral line (Ushikubo et al., 2012); others are the same as in Fig.1.

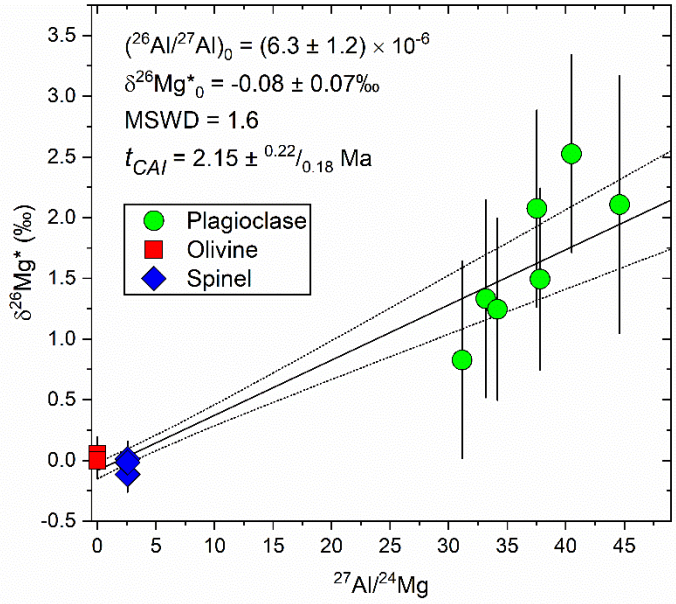

1342

1343 Fig. 7. The Al-Mg isochron diagram for the plagioclase-bearing ARC, MET 00526_A2. The solid

1344 line represents the regression, and the dashed lines are 95 % confidence intervals on the fit.

1345 Uncertainties for $(^{26}Al/^{27}Al)_0$ and $(\delta^{26}Mg^*)_0$ are 95 % confidence levels.

1346

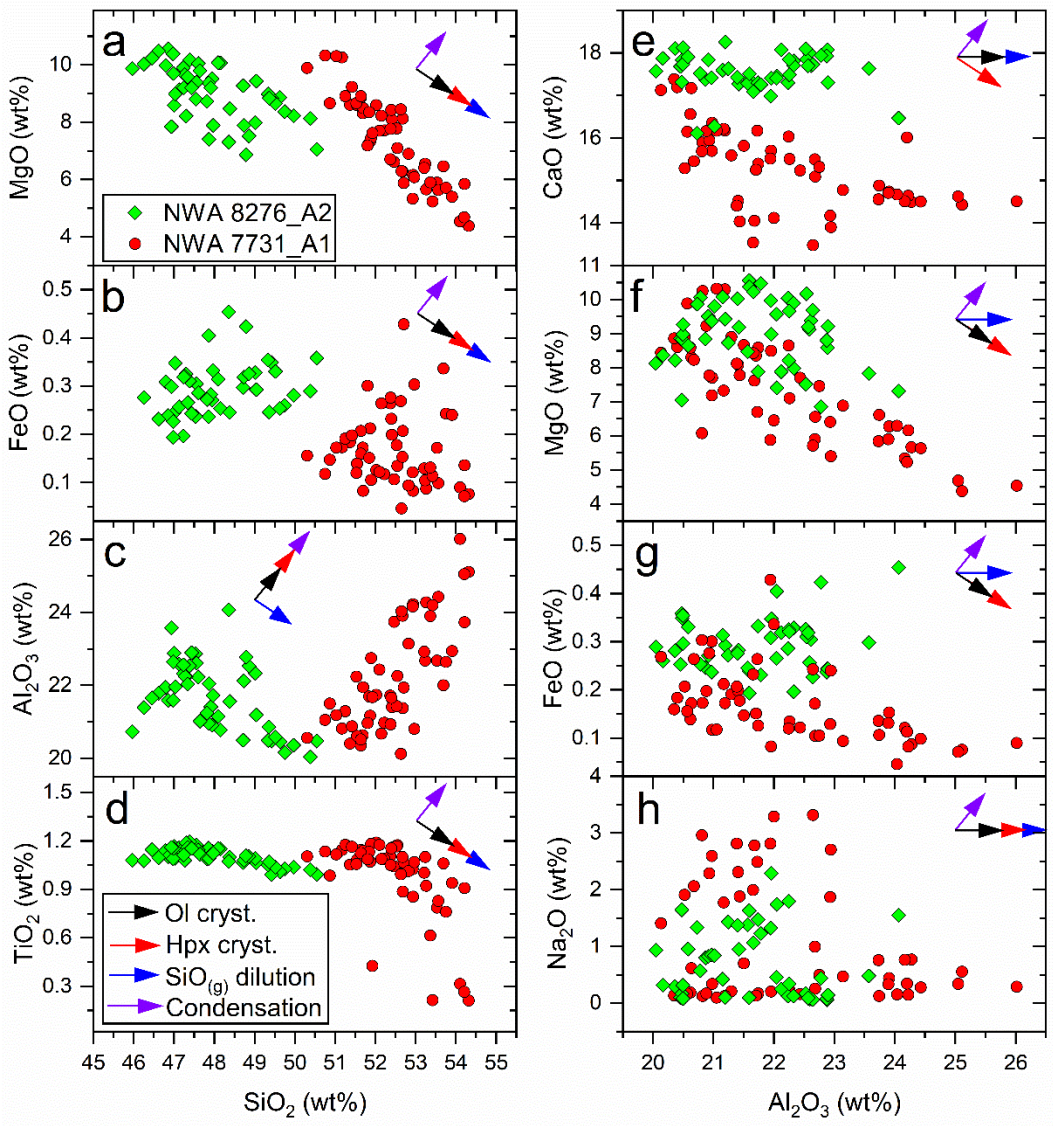

Fig. 8. Correlations of major elements in the glassy mesostasis of NWA 8276_A2 and NWA 7731_A1. The black and red arrows indicate the evolution trend of glassy mesostasis due to olivine and high-Ca pyroxene crystallization, respectively. In contrast, the blue arrow indicates the dilution effects on the concentrations of refractory elements like Al and Ti by the condensation of gaseous SiO. The purple arrow indicates the evolution trends of gaseous element condensation.

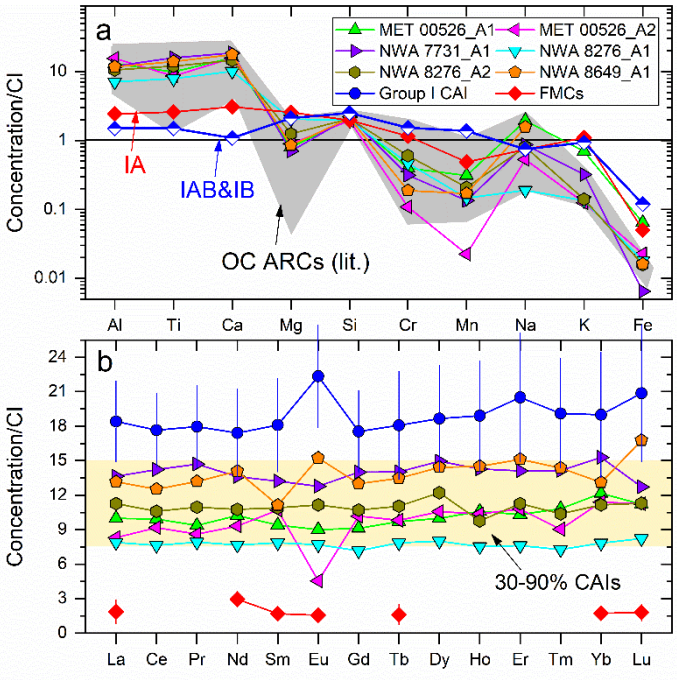

Fig. 9. Calculated bulk major and REE concentrations of OC ARCs in this study. The ranges of REE concentration in Group I CAIs and FMCs are both limited (Martin and Mason, 1974; Wänke et al., 1974; Mason and Martin, 1977; Gooding et al., 1980; Grossman and Wasson, 1982, 1983; Mason and Taylor, 1982; Kurat et al., 1984; Rubin and Pernicka, 1989; Swindle et al., 1991; Sylvester et al., 1993; Huang et al., 2012; Davis et al., 2018; Torrano et al., 2019, 2023); thus, the portions of CAI materials in the precursors of OC ARCs could be estimated using the CAI-FMC mixing model, which are within the range of 30-90% (yellow region). The bulk major element compositions of OC ARCs from the literature (Bischoff and Keil, 1984; Krot and Rubin, 1994; MacPherson and Huss, 2005; Nagahara et al., 2008; Jiang et al., 2015; Ebert and Bischoff, 2016; Ross et al., 2017; Varela and Zinner, 2018) are plotted for comparison.

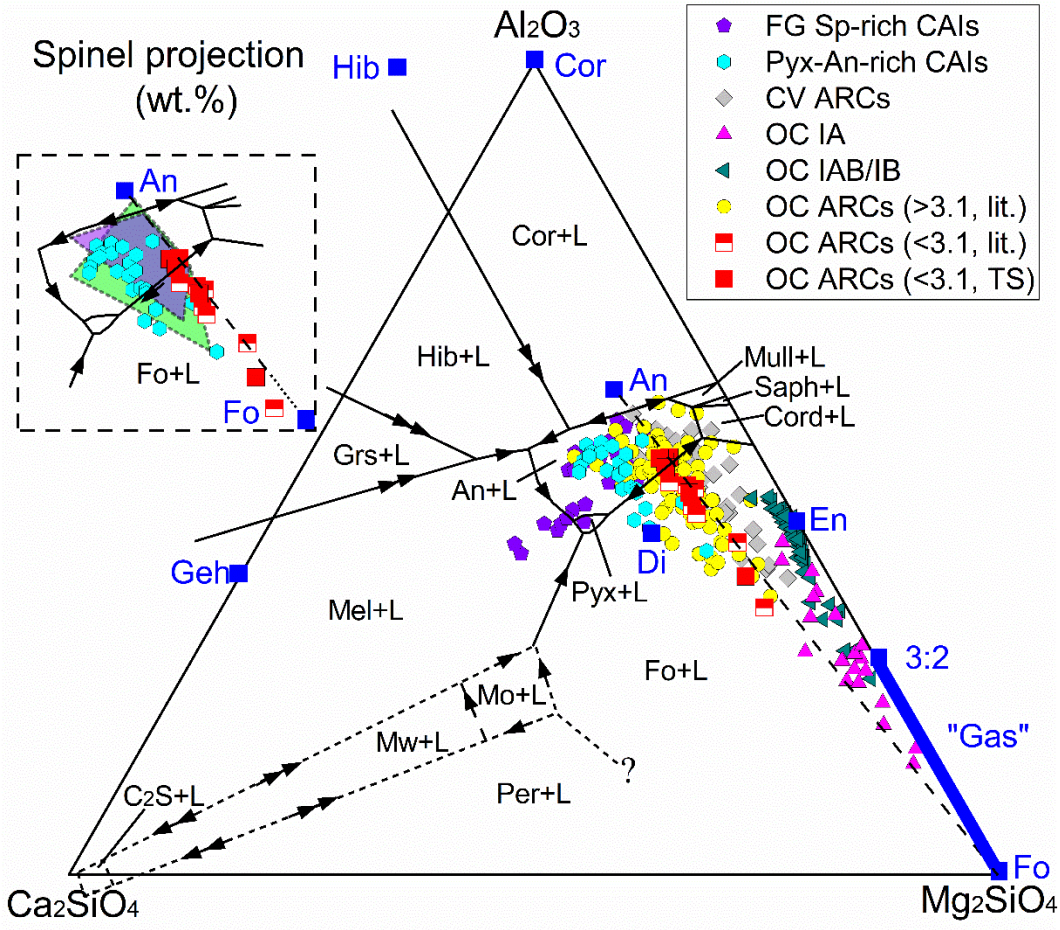

1366

1367 Fig. 10. Bulk compositions of OC ARCs, as plotted on the spinel-saturated ternary diagram of
1368 Ca_2SiO_4–Mg_2SiO_4–Al_2O_3. The phase diagram is adopted from Huss et al. (2001) and MacPherson
1369 and Huss (2005). The data of OC ARCs with petrologic type ≤3.1 are from this study and literature
1370 (Semarkona and NWA 7402; Rubin, 2004; MacPherson and Huss, 2005; Nagahara et al., 2008;
1371 Ross et al., 2017). The data of OC ARCs with petrologic type >3.1 are from Bischoff and Keil (1983),
1372 Bischoff et al. (1989), Krot and Rubin (1994), MacPherson and Huss (2005), Jiang et al. (2015),
1373 Ebert and Bischoff (2016), and Varela and Zinner (2018), with their bulk compositions corrected for
1374 Fe-Mg and (N, K)-Ca exchanges. For comparison, literature data of CV ARCs (Sheng et al., 1991;
1375 Zhang et al., 2020b), OC IA/IAB/IB chondrules (Jones and Scott, 1989; Jones, 1994; Tachibana et
1376 al., 2003; Kita et al., 2010), and CV fine-grained spinel-rich ("FG Sp-rich") CAIs (Krot et al., 2004b),
1377 and pyroxene-anorthite-rich ("Pyx-An-rich") CAIs in CV (namely type C) (Wark, 1987; Lin and Kimura,
1378 1998), CO, and Acfer 094 chondrites (Krot et al., 2004a; Zhang et al., 2020a) are plotted. The blue

segment on the Fo-Cor axis represents the composition range of ambient gas inferred from the bulk compositions trend of OC ARCs on the MgO-($CaO+Al_2O_3$)-SiO_2 diagram (Fig. S4). The green and purple regions represent the bulk compositions of CAI components in the precursors of OC ARCs calculated by assuming two endmember mixing of CAIs and type I (IA&IAB/IB) chondrule materials or CAIs and the ambient gas, respectively (Table S10b). Abbreviations: Cor = corundum; Hib = hibonite; Grs = grossite; Geh = gehlenite; Mel = melilite; An = anorthite; Pyx= pyroxene; Di = diopside; En = enstatite; Fo= forsterite; Cord= corderite; Saph = sapphirine; Mull = mullite; Mo = monticellite; Mw = merwinite.

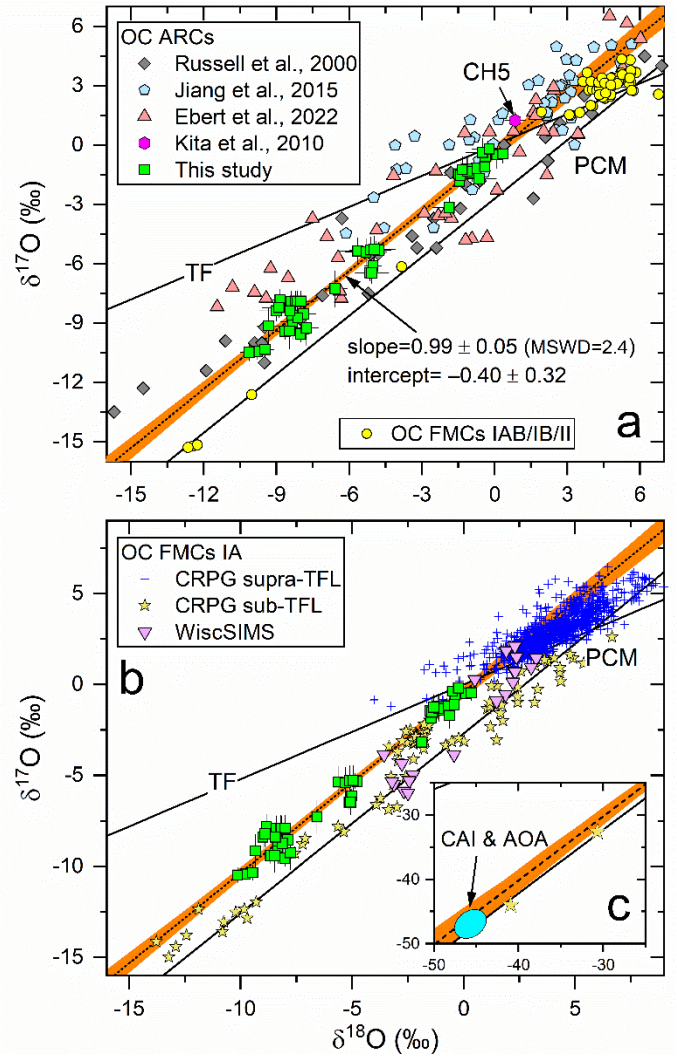

Fig. 11. The oxygen isotope mixing line of OC ARCs in this study. The equation of the mixing line is $\delta^{17}O = (0.99 \pm 0.05) \times \delta^{18}O - (0.40 \pm 0.32)$ (MSWD = 2.4). The error envelope of the mixing line is shaded in orange. In panel a, the oxygen isotope ratios of ARCs from metamorphosed OCs (Russell et al., 2000; Jiang et al., 2015; Ebert et al., 2022) and OC type IAB & B & II chondrules (Kita et al., 2010; Siron et al., 2021, 2022) are plotted for comparison. In panel b, type IA chondrules analyzed by the CRPG-CNRS group (Piralla et al., 2021; Marrocchi et al., 2024) and the WiscSIMS group (Kita et al., 2010; Siron et al., 2022) are shown in different symbols; the former was displayed in two groups, i.e., supra-TFL (terrestrial fractionation line, $\Delta^{17}O$ >0‰) and sub-TFL ($\Delta^{17}O$ <0‰), as suggested by Marrocchi et al., (2024). In panel c, the

oxygen isotope region of CAIs and AOAs are indicated along with the two AOA-like relict olivines ($\Delta^{17}O$ <–15‰) identified by Piralla et al., (2021), which are consistent with both the PCM and the OC ARC lines.

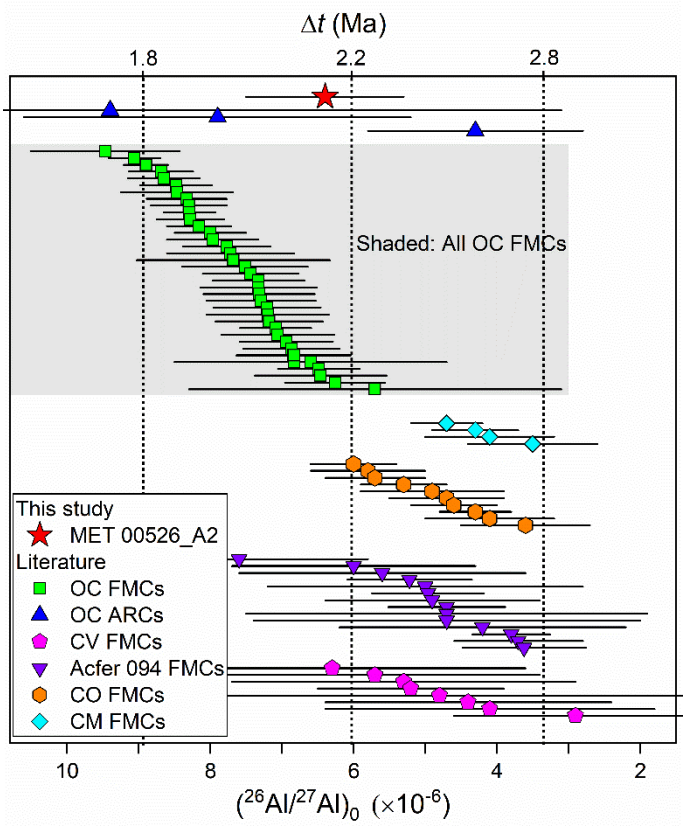

Fig. 12. Comparison of the Al-Mg age of MET 00526_A2 of this study to literature OC ARCs (Russell et al., 1996; Russell et al., 1997) and FMCs in OCs (Siron et al., 2021, 2022), COs and CMs (Fukuda et al., 2022), Acfer 094 (Ushikubo et al., 2013; Hertwig et al., 2019), and CVs (Nagashima et al., 2017). A grey shaded area represents the range of $(^{26}Al/^{27}Al)_0$ of OC (L/LL<3.1) FMCs in earlier literature (Hutcheon and Hutchison, 1989; Kita et al., 2000; Rudraswami and Goswami, 2007; Rudraswami et al., 2008; Villeneuve et al., 2009; Mishra et al., 2010; Bollard et al., 2019; Pape et al., 2019). The significant older Al-Mg ages (~0.8 Ma) of two OC FMCs determined from spinels by Piralla et al. (2023) were not plotted. If all OC FMC data are considered, MET 00526_A2 formed within the period of OC chondrule-forming events. If only OC FMC data from recent studies (Siron et al., 2021, 2022) were considered, MET 00526_A2 plots to their younger end, likely suggesting a late arrival of CAI materials from the outer solar system into the OC chondrule-forming region.

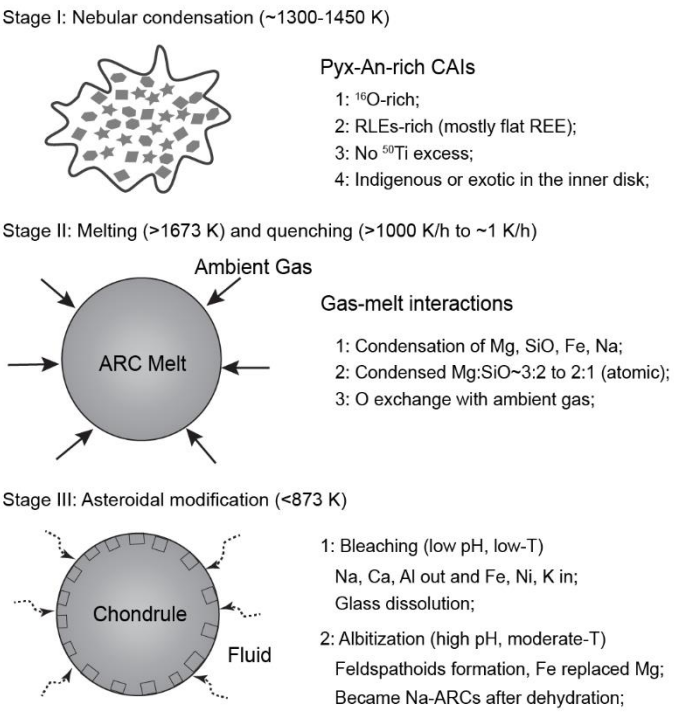

Fig. 13. Schematic diagram for the formation mechanism of OC ARCs. The cooling rates of OC ARCs are inferred from their textures, i.e., plagioclase-bearing (~10-500 K/h; Tronche et al., 2007; ~1 K/h; Wick and Jones, 2012), barred-olivine (100-7200 K/h; Lofgren and Lanier, 1990; Radomsky and Hewins, 1990; Tsuchiyama et al., 2004; or <10 K/h; Faure et al., 2022). Abbreviations: low-T: low temperature; high-T = high temperature; Na-ARCs = Na-Al-rich chondrules.

Table 1. Average major element compositions of constituent minerals determined by EPMA and the reconstructed bulk compositions of the six ARCs studied

ARC	MET 00526_A2[#]					MET 00526_A1				NWA 7731_A1				
Size (μm)	430 × 250					570 × 300				440 × 440				
Minerals	Sp (5)	Ol (5)	Hpx (4)	Pl (11)	Bulk[‡]	Ol (12)	Hpx (19)	Mes (7)*	Bulk[‡]	Sp (1)	Ol (2)	Hpx (26)	Glass (53)	Bulk[‡]
Vol%	3.2	13.6	16.7	42.1		7.7	16.1	76.2		0.0	0.1	37.5	62.3	
MgO	28.8	56.1	22.3	0.91	18.5	56.2	15.4	6.4	12.6	27.7	57.1	15.8	7.33	11.1
SiO_2	0.07	41.2	50.2	45.7	43.7	42.3	45.3	47.1	47.3	1.54	42.7	45.4	52.4	49.7
Al_2O_3	70.4	0.14	5.62	34.0	22.0	0.29	13.5	24.4	20.7	69.2	0.19	15.3	22.2	19.4
CaO	0.03	0.36	17.4	18.7	13.9	0.42	21.6	14.8	15.1	0.74	0.34	20.7	15.3	17.7
FeO	0.23	0.46	0.66	0.44	0.56	0.75	0.65	1.78	1.51	0.11	0.28	0.11	0.19	0.15
Na_2O			0.01	0.60	0.30		0.05	1.84	1.37			0.03	1.04	0.61
TiO_2	0.44	0.15	3.02		0.85	0.13	1.98	0.45	0.72	0.41	0.13	1.40	0.98	1.16
Cr_2O_3	0.14	0.09	0.11		0.05	0.15	0.25	0.12	0.15	0.23	0.14	0.17	0.08	0.12
V_2O_3	0.15		0.12		0.05		0.08	0.03	0.04	0.31		0.09	0.06	0.07
NiO		0.09	0.20		0.10	0.11	0.16	0.47	0.39		0.01	0.02	0.03	0.03
MnO	0.01	0.05	0.03		0.01	0.08	0.06	0.08	0.08		0.05	0.02	0.04	0.03
ZnO	0.06				0.00					0.05				0.00
Total	100.3	98.7	99.6	100.4	100.0	100.4	99.1	97.5	100.0	100.3	100.9	99.2	99.7	100.0

ARC	NWA 8276_A1					NWA 8276_A2				NWA 8649_A1			
Size (μm)	1100 × 700					580 × 580				200 × 200			
Minerals	Sp (6)	Ol (9)	Hpx (6)	Mes (10)*	Bulk[‡]	Ol (10)	Hpx (4)	Glass (49)	Bulk[‡]	Ol (2)	Hpx (11)	Glass (11)	Bulk[‡]
Vol%	0.7	43.5	1.0	54.8		19.7	0.2	80.1		10.1	14.5	75.4	
MgO	28.9	57.2	18.5	10.1	32.6	57.2	14.4	8.95	19.8	56.5	14.4	6.32	13.5
SiO_2	0.08	42.6	48.6	47.3	44.8	42.6	45.4	48.1	47.1	41.4	44.9	49.4	48.3
Al_2O_3	70.7	0.23	8.7	20.7	11.4	0.23	14.6	21.7	17.0	0.08	16.2	22.1	18.9
CaO	0.05	0.64	20.2	18.3	9.88	0.64	22.2	17.5	13.9	0.34	21.8	17.7	16.7
FeO	0.48	0.47	0.37	0.38	0.42	0.47	0.37	0.34	0.37	0.32	0.34	0.39	0.38
Na_2O			0.02	0.26	0.13		0.02	0.73	0.57		0.02	1.51	1.10
TiO_2	0.25	0.07	1.47	1.03	0.58	0.07	1.53	1.10	0.88	0.09	1.65	1.00	1.02
Cr_2O_3	0.23	0.12	0.32	0.23	0.18	0.12	0.49	0.26	0.23	0.05	0.10	0.07	0.07
V_2O_3	0.35		0.07	0.05	0.03		0.09	0.06	0.04		0.07	0.03	0.03
NiO		0.05	0.05	0.04	0.04	0.05	0.04	0.09	0.08	0.04	0.04	0.07	0.06
MnO	0.01	0.03	0.07	0.04	0.04	0.03	0.07	0.06	0.05	0.04	0.03	0.05	0.04
ZnO	0.03				0.00				0.00				0.00

Total	101.1	101.4	98.4	98.5	100.0	101.4	99.2	98.9	100.0	98.8	99.5	98.5	100.0

[#]MET 00526_A2 contains 15.7 area% Na-Cl-bearing phases attributed to parent body alteration and has not been included in bulk composition calculation; *Compositions of mesostasis were obtained using a defocused beam (15 μm). The numbers in brackets represent the number of analyses for each mineral. Individual analysis result can be found in Table S2. ǂ Bulk composition of a chondrule was recalculated from its modal mineral abundance (in wt%) and average mineral compositions; Abbreviations: Sp = spinel; Ol = olivine; Hpx = high-Ca pyroxene; Pl = plagioclase; Mes = mesostasis.

Table 2. Average trace element concentrations of constituent minerals determined by LA-ICP-MS and the reconstructed bulk trace element compositions of the six ARCs studied

ARCs	MET 00526_A1			MET 00526_A2			NWA 7731_A1	NWA82 76_A1	NWA82 76_A2	NWA86 49_A1	Group I CAI		OC FMCs	
	Hpx	Mes	Bulk	Na-rich	Mes	Bulk					Mean	SD	Mean	SD
N	2	3	5	4	4	8	6	6	23	3	33		165	
Zr	42.5	40.9	37.6	7.0	66.8	52.7	47.8	24.6	40.8	47.8				
Hf	1.6	1.1	1.1	0.2	1.9	1.5	1.4	0.6	1.2	1.4				
Sc	149	48.0	62.8	5.2	108	84.9	83.9	43.2	63.9	93.2				
Y	23.1	13.8	14.3	1.8	24.6	19.4	19.9	10.3	15.2	19.9				
Ti	11828	4208	5448	645	9661	7640	7185	3382	5492	6278				
Sr	8.7	83.7	62.2	71.2	39.8	31.4	97.7	51.3	74.1	114.6				
Ba	0.3	17.2	12.5	10.1	9.7	7.6	30.8	16.2	21.2	29.9				
V	240.0	29.3	66.6	22.4	17.2	18.1	178.3	67.3	99.9	25.3				
Cr	1863	1274	1279	82	787	635	1011	1057	1573	445				
Mn	448	875	743	90	229	183	370	383	495	212				
Rb	0.2	2.7	2.0	3.2	3.1	2.4	0.0	0.1	0.7	0.1				
La	1.0	2.8	2.2	0.5	3.3	2.6	3.2	1.7	2.5	3.0	4.2	0.7	0.44	0.24
Ce	3.6	7.3	6.0	1.6	9.7	7.6	8.8	4.4	6.3	7.7	10.8	1.6		
Pr	0.8	1.0	0.9	0.2	1.4	1.1	1.4	0.7	1.0	1.2	1.6	0.3		
Nd	4.7	5.2	4.6	0.9	7.2	5.7	6.2	3.2	4.7	6.3	7.4	1.4	1.35	0.31
Sm	2.0	1.4	1.4	0.1	2.6	2.1	1.9	1.0	1.5	1.6	2.5	0.5	0.25	0.08
Eu	0.0	0.6	0.5	0.6	0.4	0.3	0.7	0.4	0.6	0.8	1.2	0.2	0.09	0.03
Gd	2.5	1.8	1.8	0.6	3.4	2.7	2.8	1.3	2.0	2.5	3.2	0.4		
Tb	0.6	0.3	0.4	0.0	0.6	0.5	0.5	0.3	0.4	0.5	0.6	0.1	0.06	0.03
Dy	4.0	2.3	2.4	0.3	4.3	3.4	3.6	1.7	2.8	3.4	4.2	0.9		
Ho	0.9	0.6	0.6	0.1	1.0	0.8	0.8	0.4	0.5	0.8	1.0	0.2		
Er	2.7	1.6	1.7	0.2	3.0	2.3	2.3	1.1	1.8	2.4	3.1	0.7		
Tm	0.4	0.3	0.3	0.0	0.4	0.3	0.3	0.2	0.2	0.3	0.4	0.1		
Yb	3.1	2.0	2.0	0.2	3.2	2.5	2.5	1.2	1.7	2.1	2.9	0.7	0.28	0.10
Lu	0.4	0.3	0.3	0.0	0.5	0.4	0.3	0.2	0.3	0.4	0.7	0.5	0.05	0.07
CAI %[a]		40-75			30-75		40-100	25-60	40-80	50-80				
Low limit[c]		~80			~75		~80	~45	~65	~75				

[a]: The portion of CAIs in the precursor of OC ARCs was estimated from their trace element concentrations using the "CAI-FMC hybrid" model and the "CAI + Gas" model (Table S10a). [b]: The low limit of the CAIs portion in the precursor of OC ARCs is estimated from their major element contents using the "CAI-FMC hybrid" and the "CAI-Gas" models (Table S10b). Individual analysis result can be found in Table S3. Data source for group I CAIs is: Martin and Mason (1974), Wänke et al. (1974), Mason and Martin (1977), Mason and Taylor (1982), Sylvester et al. (1993), Huang et al. (2012), Davis et al. (2018), and Torrano et al. (2019, 2023). Data source for OC FMCs is: Gooding et al. (1980), Grossman and Wasson (1982, 1983), Kurat et al. (1984), Rubin and Pernicka (1989), and Swindle et al. (1991).

Table 3. Oxygen isotope ratios of major minerals in the six ARCs studied

Chondrule	Texture	Spot	Mineral	$\delta^{18}O$	Unc.	$\delta^{17}O$	Unc.	$\Delta^{17}O$	Unc.
Heterogeneous chondrules									
MET 00526_A2[#]	Porphyritic	#1a	Sp	-9.8	0.4	-10.4	0.4	-5.3	0.3
		#2a	Sp	-10.1	0.4	-10.5	0.4	-5.2	0.3
		#3a	Ol	-8.7	0.4	-9.4	0.4	-4.9	0.3
		#4a	Ol	-9.5	0.4	-10.3	0.4	-5.4	0.3
		#6b	Ol	-9.3	0.5	-9.1	0.9	-4.3	0.9
		#1b	Hpx	-8.3	0.5	-8.9	0.9	-4.6	0.9
		#2b	Hpx	-8.5	0.5	-9.4	0.9	-5.0	0.9
		#5b	Hpx	-8.3	0.5	-8.6	0.9	-4.3	0.9
		#8b	Hpx	-7.9	0.5	-8.5	0.9	-4.4	0.9
		#5a	Pl	-5.1	0.4	-6.5	0.4	-3.8	0.3
		#6a	Pl	-5.0	0.4	-6.1	0.4	-3.5	0.3
		#7a	Pl	-8.0	0.4	-9.6	0.4	-5.4	0.3
		#3b	Pl	-7.8	0.5	-9.3	0.9	-5.2	0.9
		#4b	Pl	-8.1	0.5	-8.7	0.9	-4.5	0.9
		#7b	Pl	-6.6	0.5	-7.3	0.9	-3.9	0.9
NWA 8649_A1	Glassy	#1	Gl	-0.6	0.7	-1.7	0.5	-1.4	0.3
		#2	Gl	-5.1	0.7	-6.5	0.5	-3.8	0.3
		#3	Gl	-1.9	0.7	-3.2	0.5	-2.2	0.3
Homogeneous chondrules									
NWA 8276_A2[*]	Glassy	#5	Gl (Altered)	4.2	0.7	2.7	0.7	0.5	0.4
		#6	Gl (Altered)	4.7	0.7	3.3	0.7	0.9	0.4
		Host (2Ol, 2Gl)[‡]		-0.2	0.5	-0.4	0.5	-0.3	0.3
NWA 8276_A1	Glassy	Host (2Sp, 3Ol, 2Hpx, 3Gl)[‡]		-1.0	0.5	-1.3	0.4	-0.8	0.2
MET 00526_A1	Glassy	Host (2Ol, 4Hpx)[‡]		-5.1	0.6	-5.3	0.4	-2.7	0.2
NWA 7731_A1	Glassy	Host (3Hpx, 5Gl)[‡]		-8.5	0.5	-8.1	0.3	-3.6	0.2

#: MET 00526_A2 has been analyzed in the Jul. 2021 session (12 μm, "a") and the Sep. 2021 session (3 μm, “b"); *: Two analyses on the mottled regions (likely altered) of NWA 8276_A2 have distinct oxygen isotope ratios compared to others on clean regions; ‡: the number in the brackets represents the number of analyses for each mineral; Unc. = uncertainty, other abbreviations are the same as previous. Instrumental bias correction, data reduction, and data summary can be found in tables S4, S5, and S6, respectively.

Table 4. Al-Mg isotope data of MET 00526_A2

Mineral	No.	$^{27}Al/^{24}Mg$	2SE	($\delta^{26}Mg$)*	2SE
Ol	#1	6.00E-03	1.07E-03	0.05	0.15
	#2	4.15E-03	7.37E-04	0.00	0.15
Sp	#1	2.57	2.62E-02	-0.11	0.15
	#2	2.58	2.63E-02	0.01	0.15
	#3	2.57	2.62E-02	-0.02	0.15
Pl	#1	33.2	0.42	1.33	0.81
	#2	31.1	0.39	0.83	0.81
	#3	37.5	0.49	2.08	0.81
	#4	44.6	0.54	2.11	1.06
	#6	34.1	0.40	1.25	0.75
	#8	37.8	0.46	1.49	0.75
	#9	40.5	0.52	2.53	0.81

abbreviations are the same as previous. Instrumental bias correction and data reduction details can be found in tables S7-S9.